

## RESEARCH ARTICLE

10.1002/2017JD026831

## Special Section:

Studies of Emissions and Atmospheric Composition, Clouds and Climate Coupling by Regional Surveys, 2013 (SEAC4RS)

## Key Points:

- A plume containing highly elevated water vapor concentrations was observed in situ in the stratosphere over the U.S. in summer
- Using a combination of diverse data sets, the observed enhancement in stratospheric humidity is linked to a deep convective storm system
- The quantity of water vapor irreversibly delivered to the lower stratosphere by this convective storm system is calculated

## Supporting Information:

- Supporting Information S1
- Movie S1

## Correspondence to:

J. B. Smith,  
jsmith@huarp.harvard.edu

## Citation:

Smith, J. B., et al. (2017), A case study of convectively sourced water vapor observed in the overworld stratosphere over the United States, *J. Geophys. Res. Atmos.*, 122, doi:10.1002/2017JD026831.

Received 23 MAR 2017

Accepted 7 AUG 2017

Accepted article online 18 AUG 2017

©2017. American Geophysical Union.  
All Rights Reserved.

## A case study of convectively sourced water vapor observed in the overworld stratosphere over the United States

Jessica B. Smith<sup>1</sup> , David M. Wilmoth<sup>1,2</sup> , Kristopher M. Bedka<sup>3</sup> , Kenneth P. Bowman<sup>4</sup> , Cameron R. Homeyer<sup>5</sup> , John A. Dykema<sup>1</sup>, Maryann R. Sargent<sup>1</sup>, Corey E. Clapp<sup>2</sup> , Stephen S. Leroy<sup>1</sup> , David S. Sayres<sup>1</sup> , Jonathan M. Dean-Day<sup>6</sup> , T. Paul Bui<sup>7</sup>, and James G. Anderson<sup>1,2,8</sup>

<sup>1</sup>Harvard John A. Paulson School of Engineering and Applied Sciences, Harvard University, Cambridge, Massachusetts, USA, <sup>2</sup>Department of Chemistry and Chemical Biology, Harvard University, Cambridge, Massachusetts, USA, <sup>3</sup>NASA Langley Research Center, Hampton, Virginia, USA, <sup>4</sup>Department of Atmospheric Sciences, Texas A&M University, College Station, Texas, USA, <sup>5</sup>School of Meteorology, University of Oklahoma, Norman, Oklahoma, USA, <sup>6</sup>Bay Area Environmental Research Institute, Petaluma, California, USA, <sup>7</sup>NASA Ames Research Center, Moffett Field, California, USA, <sup>8</sup>Department of Earth and Planetary Sciences, Harvard University, Cambridge, Massachusetts, USA

**Abstract** On 27 August 2013, during the Studies of Emissions and Atmospheric Composition, Clouds and Climate Coupling by Regional Surveys field mission, NASA's ER-2 research aircraft encountered a region of enhanced water vapor, extending over a depth of approximately 2 km and a minimum areal extent of 20,000 km<sup>2</sup> in the stratosphere (375 K to 415 K potential temperature), south of the Great Lakes (42°N, 90°W). Water vapor mixing ratios in this plume, measured by the Harvard Water Vapor instrument, constitute the highest values recorded in situ at these potential temperatures and latitudes. An analysis of geostationary satellite imagery in combination with trajectory calculations links this water vapor enhancement to its source, a deep tropopause-penetrating convective storm system that developed over Minnesota 20 h prior to the aircraft plume encounter. High resolution, ground-based radar data reveal that this system was composed of multiple individual storms, each with convective turrets that extended to a maximum of ~4 km above the tropopause level for several hours. In situ water vapor data show that this storm system irreversibly delivered between 6.6 kt and 13.5 kt of water to the stratosphere. This constitutes a 20–25% increase in water vapor abundance in a column extending from 115 hPa to 70 hPa over the plume area. Both in situ and satellite climatologies show a high frequency of localized water vapor enhancements over the central U.S. in summer, suggesting that deep convection can contribute to the stratospheric water budget over this region and season.

### 1. Introduction

Water vapor in the upper troposphere and lower stratosphere (UTLS) is important both radiatively and chemically. The flux of outgoing longwave radiation is especially sensitive to water vapor concentrations in the UTLS [Held and Soden, 2000], with increases leading to cooling at these levels and warming at the surface [Forster and Shine, 1999, 2002]. Indeed, Solomon et al. [2010] proposed that variability in lower stratospheric water vapor concentrations has had a measurable influence on global surface temperature trends. Additionally, the results of an analysis by Dessler et al. [2013] suggest that stratospheric water vapor may constitute a positive feedback in the climate system, whereby a warmer climate leads to increases in stratospheric water vapor concentrations, which then contribute to further warming. Their estimates of the magnitude of this feedback in W/m<sup>2</sup> per degree warming indicate that stratospheric water vapor may be important in determining the sensitivity of the climate system.

Water vapor is also integral to stratospheric chemistry as it is the dominant source of OH in the lower stratosphere [Hanisco et al., 2001]. Furthermore, increases in stratospheric water vapor concentrations can enhance the rates of several heterogeneous reactions that amplify stratospheric ozone loss by promoting the uptake, growth, and dilution of the ubiquitous sulfuric acid aerosol [Carslaw et al., 1995; Carslaw et al., 1997]. Given sufficient surface area and sulfate dilution, these liquid aerosols can become highly efficient catalysts for the heterogeneous conversion of inorganic chlorine reservoir species to their catalytically active free radical forms [e.g., Shi et al., 2001; Hanisco et al., 2002; Drdla and Müller, 2012; Anderson et al., 2012, 2017].

Despite the well-documented importance of UTLS water vapor to atmospheric chemistry and climate, the processes that control its distribution in this region are not well understood. This is especially true in the extra-tropics where several different dynamical mechanisms are capable of influencing UTLS water vapor concentrations [Weinstock *et al.*, 2007; Pittman *et al.*, 2007; Ploeger *et al.*, 2013]. The primary mechanism by which air and water vapor enter the stratosphere, i.e., the Brewer-Dobson circulation (BDC), is characterized by air gradually ascending across the tropical tropopause, and then progressing upward and poleward toward higher latitudes, where it descends and reenters the troposphere [Brewer, 1949; Holton *et al.*, 1995; Holton and Gettelman, 2001]. As air ascends through the tropical tropopause layer, water vapor in excess of the saturation mixing ratio condenses and is removed by sedimentation [Jensen and Pfister, 2004; Fueglistaler *et al.*, 2005, 2009; Schoeberl and Dessler, 2011]. Though there is debate regarding the efficiency of this mechanism [Jensen *et al.*, 2005, 2013; Fueglistaler *et al.*, 2014; Schoeberl *et al.*, 2014; Rollins *et al.*, 2016], tropical tropopause temperatures account for the typically dry conditions of the stratosphere, as well as the annual cycle observed in stratospheric water vapor concentrations. When tropical tropopause temperatures are colder in the winter, water vapor concentrations in the lower tropical stratosphere are lower, and when tropical tropopause temperatures are warmer in the summer, water vapor concentrations are higher [e.g., Mote *et al.*, 1996]. The signature of this annual cycle persists as the air rises and moves poleward with the BDC.

Extra-tropical tropopause-penetrating convection, the pathway under consideration here, provides a means of directly injecting air and water, predominantly as ice, into both the middleworld stratosphere (altitudes between the local tropopause level and the nominal level of the tropical tropopause at 380 K potential temperature) and overworld stratosphere (>380 K potential temperature) [Hoskins, 1991; Dessler *et al.*, 1995]. In contrast to the slow ascent associated with the BDC, the convective mechanism effectively bypasses the thermal control of tropical cold-point tropopause temperatures [Dessler and Sherwood, 2004]. In the following analysis, we focus specifically on deep convective storm systems that occur over the Contiguous U.S. (CONUS) during the summer and their impact on stratospheric water vapor concentrations over this region and season.

Fundamentally, convection arises from the temperature difference between a parcel of warm air and the cooler air surrounding it. Warm air, which is less dense, i.e., more buoyant, rises through the atmospheric column and adiabatically expands and cools. When the temperature of the rising air parcel has cooled sufficiently, the water vapor it contains will begin to condense and release energy (latent heat). This addition of heat leads to further warming and facilitates the continued ascent of the parcel. If the surrounding atmosphere cools quickly with height, it leads to unstable conditions, and the parcel will continue to rise until it is at the same temperature as the environment, a level known as the equilibrium level, where it becomes neutrally buoyant. This level is often near the tropopause. The anvil structure at the top of deep convective storms is indicative of the level where the rising motion is stopped, and the mass has spread out horizontally. If parcels within the convective core have enough upward momentum, however, as in the case of overshooting tops (OTs), they can continue to rise past their equilibrium level and penetrate into the stratosphere by crossing the local tropopause level. The rising motion will continue until negative buoyancy in the stratosphere decelerates these overshooting parcels. The vast majority of the mass transported vertically in convective overshoots rapidly descends back toward the equilibrium level in the upper troposphere. A fraction, however, can detrain in the stratosphere via gravity wave breaking and turbulent mixing with stratospheric air [Wang, 2003; Mullendore *et al.*, 2005; Grosvenor *et al.*, 2007; Homeyer *et al.*, 2014a; Wang *et al.*, 2011; Homeyer *et al.*, 2017]. These diabatic processes increase the potential temperature of the overshooting parcel, making it neutrally buoyant at stratospheric altitudes, and result in the irreversible delivery of tropospheric air and moisture to the stratosphere [Mullendore *et al.*, 2005; Homeyer *et al.*, 2014a, 2017].

Convective overshoots that penetrate the tropopause in both the tropics and the extra-tropics have the potential to increase the humidity of the stratosphere, including the stratospheric overworld, through the rapid sublimation of convectively lofted ice. This has been demonstrated in both modeling (tropics: Grosvenor *et al.* [2007], Jensen *et al.* [2007], and Dessler *et al.* [2007]; extra-tropics: Wang [2003], Dessler and Sherwood [2004], Le and Gallus [2012], and Homeyer *et al.* [2017]) and observational studies (tropics: Kley *et al.* [1982], Corti *et al.* [2008], de Reus *et al.* [2009], Khaykin *et al.* [2009], Iwasaki *et al.* [2010], Sayres *et al.* [2010], Sargent *et al.* [2014], and Khaykin *et al.* [2016]; extra-tropics: Poulida *et al.* [1996], Hegglin *et al.*

[2004], Ray *et al.* [2004], Hanisco *et al.* [2007], Weinstock *et al.* [2007], and Homeyer *et al.* [2014b, 2017]). Most of the water carried aloft in OTs is bound in the solid phase as ice, with the partitioning between the ice and vapor phases determined by the very cold temperatures attained within these rapidly rising air masses [Jensen *et al.*, 2007]. Even a small volume of tropospheric air can carry a significant quantity of water in the condensed phase. Mixing of tropospheric air with the surrounding stratosphere, which is typically subsaturated [Smith *et al.*, 2001], facilitates the rapid sublimation of convectively lofted ice. The expected lifetime for ice in this dry environment, especially for particles with diameters  $<20\ \mu\text{m}$ , is short [Jensen *et al.*, 2007], and as the ice sublimates, it moves the stratosphere toward saturation. The resulting mixed parcel, often evident in observational data as a discrete plume, will exhibit a larger fractional change in water vapor than in other long-lived trace species [e.g., Dessler and Sherwood, 2004].

The net contribution of deep tropopause-penetrating convection to stratospheric water vapor concentrations is not well understood and is not well represented in global models because of the small spatial scales and short time scales over which convection occurs. However, the model and measurement studies cited above, and the results of this work, show that localized deep convective events can impact the chemical composition, in particular the moisture levels, of the stratosphere. Deep convection may also facilitate the rapid transport of boundary layer species directly to the overworld stratosphere (model: Stenchikov *et al.* [1996] and Mullendore *et al.* [2005]; observations: Fischer *et al.* [2003], Jost *et al.* [2004], and Ray *et al.* [2004]), possibly including halogen precursors implicated in stratospheric ozone loss [Liang *et al.*, 2014]. Given the potential for changes to both convective frequency and strength in response to anthropogenic climate forcing [Trapp *et al.*, 2007, 2009; Van Klooster and Roebber, 2009; Booth *et al.*, 2012], it is imperative that this convective term be well characterized for incorporation into prognostic coupled chemistry-climate models.

In the following analysis, we begin by showing the in situ record of encounters with plumes in the stratosphere characterized by large localized enhancements in water vapor, with a focus on those observed in the overworld. The data were acquired by the Harvard Water Vapor instrument, flown aboard NASA's WB-57 and ER-2 aircraft, over a decade of missions targeting the central and south-central U.S. in summer. Within this framework, we highlight the results of a singular plume observed on the ER-2 flight of 27 August 2013, during the Studies of Emissions and Atmospheric Composition, Clouds and Climate Coupling by Regional Surveys (SEAC<sup>4</sup>RS) campaign in the summer of 2013. Next we identify the storm system that was the likely source for this plume through a strategic combination of diverse data types and provide a quantitative estimate of the water vapor irreversibly delivered to the overworld stratosphere via the this storm system. Finally, utilizing both aircraft and satellite climatologies, we discuss the impact of tropopause-penetrating convection on water vapor concentrations in the stratosphere within a larger seasonal and regional context.

## 2. In Situ Observations of Convectively Sourced Plumes Over North America

### 2.1. Harvard Water Vapor Instrument

Aircraft data provide high spatial and temporal resolution measurements at a scale (1 Hz or a horizontal resolution of  $\sim 200\ \text{m}$ ) that is well matched to the scale of convectively sourced water vapor plumes, which have been observed to be a few hundred kilometers in horizontal extent and up to  $\sim 2\ \text{km}$  in vertical depth hours to days after the convective event. Simultaneous in situ measurements of the atmospheric state variables and trace species reveal the physical and chemical properties of the background atmosphere, as well as the composition within these plumes in the UTLS. For this analysis, we use water vapor measured by the Harvard Water Vapor instrument (HWV) and temperature and pressure obtained by the onboard Meteorological Measurement System [Scott *et al.*, 1990; Gaines *et al.*, 1992]. The data, constrained primarily by limitations in aircraft flight tracks, provide detailed information regarding the precise geographic location and altitude of these plumes, their physical size, the magnitude of the moisture enhancement above the background concentration, and additional chemical signatures arising from the mixing of tropospheric and stratospheric air parcels associated with tropopause-penetrating storms.

HWV has a long history of acquiring data in situ in the UTLS aboard both NASA's ER-2 and WB-57 aircraft [Weinstock *et al.*, 1994; Hintsa *et al.*, 1999; Weinstock *et al.*, 2006a, 2006b, 2009; Sargent *et al.*, 2013]. The current version of the instrument, first flown in 2011, combines two independent measurement methods for the simultaneous detection of ambient water vapor mixing ratios within a shared duct

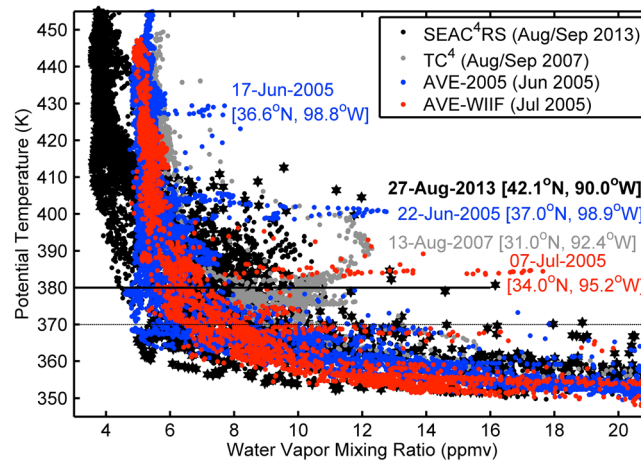


**Figure 1.** In situ water vapor data as a function of potential temperature. Water vapor was measured in situ by HWV (10 s) over the central and south-central U.S. during four summertime airborne missions: Aura Validation Experiment Summer 2005 (AVE-2005), AVE-Water Isotope Intercomparison Flights (AVE-WIIF), Tropical Composition, Cloud and Climate Coupling (TC<sup>4</sup>), and SEAC<sup>4</sup>RS. Extreme moist plume encounters are labeled by flight day. The starred points denote the plume encountered north of 40°N on the flight 27 August 2013 during the SEAC<sup>4</sup>RS mission. The horizontal solid black line indicates the 380 K level, the lower boundary of the overworld, and the dashed black line indicates the 370 K level, representative of the typical tropopause level for summertime missions over the U.S.

HITRAN spectral parameters [Rothman *et al.*, 2009] and validated through comparisons with the Harvard laboratory calibration system [Sargent *et al.*, 2013]. The precision is typically better than 0.2 ppmv (Ly- $\alpha$ ) and 0.01 ppmv (HHH) in 1 s data, and additional laboratory tests constrain biases in the Ly- $\alpha$  and HHH detection axes to less than  $\pm 0.3$  ppmv [Hintsa *et al.*, 1999; Smith, 2012; Sargent *et al.*, 2013]. In summary, the Harvard Water Vapor (HWV) instrument is well suited to resolve the highly localized changes in ambient water vapor associated with convective detrainment in the UTLS.

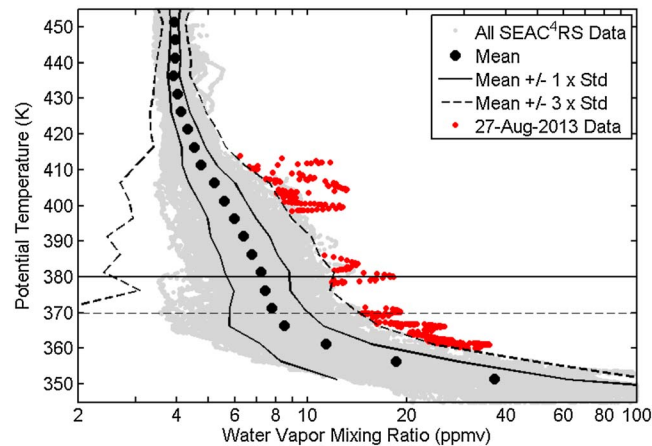
## 2.2. In Situ Record of Convectively Sourced Plume Encounters

Figure 1 shows in situ measurements of water vapor mixing ratio, measured by HWV (10 s data), as a function of potential temperature. The data shown here were obtained aboard NASA's WB-57 and ER-2 aircraft north of 25°N over the central U.S. during four missions that were staged out of Houston, TX, over the past decade. Several distinct enhancements in water vapor, potentially tied to tropopause-penetrating convection, are apparent in the data set. Water vapor mixing ratios in these moist plumes are elevated by more than  $3\sigma$  above the nominal 4–6 ppmv background. Individual plume encounters in the overworld are color-coded by mission and labeled by flight date. The latitude and longitude coordinates for each encounter are also indicated. The 370 K potential temperature surface, which is representative of the typical tropopause level for summertime missions over the U.S., and the 380 K surface, which marks the boundary between the middleworld and overworld stratosphere, are shown for reference. What is noteworthy about these plumes is (1) the magnitude of the enhancements, up to 12 ppmv above the background in the overworld, and (2) the altitudes within the stratospheric overworld at which they were observed, up to nearly 440 K (~19 km).

During missions prior to the SEAC<sup>4</sup>RS campaign, the moist plumes evident in Figure 1 were encountered serendipitously and were not intentional targets of study. In contrast, SEAC<sup>4</sup>RS explicitly sought to characterize the impact of deep convection on the chemical composition of the UTLS and overworld stratosphere [Toon *et al.*, 2016]. Indeed, with peak 10 s values between 10 and 16 ppmv, the plume encounter on 27 August 2013 during SEAC<sup>4</sup>RS (black stars) represents the highest mixing ratios ever observed in situ at these potential temperatures (380–415 K) and latitudes (>40°N).

[Sargent *et al.*, 2013]. This dual-axis instrument combines the heritage of the Harvard Lyman- $\alpha$  photofragment fluorescence instrument (Ly- $\alpha$ ) with a custom tunable diode laser direct-absorption instrument, the Harvard Herriott Hygrometer (HHH). The observed agreement between these axes provides a stringent constraint on the accuracy of the measurements in both the laboratory and flight environments.

The dual-axis HWV instrument obtains 1 s measurements of ambient water vapor mixing ratios from ~1 to ~500 ppmv. The typical measurement accuracy for Ly- $\alpha$  (5–10%  $1\sigma$ ) is determined through laboratory calibration and is validated in-flight at mixing ratios >100 ppmv by direct UV absorption across the instrument duct [Hintsa *et al.*, 1999; Weinstock *et al.*, 2006a, 2009; Smith, 2012]. The accuracy of HHH (5–10%  $1\sigma$ ) is calculated from the uncertainties in



**Figure 2.** SEAC<sup>4</sup>RS water vapor data as a function of potential temperature. Water vapor was measured in situ by HWV (1 s) over the central U.S. during SEAC<sup>4</sup>RS. The mission-wide mean profile is plotted in the solid black circles. Also shown are the mean  $\pm$  one and three standard deviations (solid and dashed wavy black lines). The majority of the values in excess of  $3\sigma$  (extrema) were encountered on the 27 August 2013 flight (solid red circles). The horizontal solid black line indicates the 380 K level, the lower boundary of the overworld, and the horizontal dashed black line indicates the 370 K level, which corresponds to the tropopause level throughout SEAC<sup>4</sup>RS. Note the logarithmic scale on the x axis.

American Monsoon upper level Anticyclone (NAMA) [Gill, 1980; Dunkerton, 1995], in determining the chemical composition of the UTLS. In total, seven flights during SEAC<sup>4</sup>RS targeted the NAMA specifically, with an additional nine flights targeting the vertical distribution of trace species within the UTLS as well as the influence of convection on the stratosphere.

Figure 2 shows the vertical distribution of water vapor, as measured by HWV (1 s data), throughout the UTLS for the entire SEAC<sup>4</sup>RS period. Together, Figures 1 and 2 capture two important features of the humidity structure of the summertime stratosphere over CONUS: (1) a broad region of increased variability and seasonally enhanced ( $>6$  ppmv) moisture (*bump*) in the stratosphere between the nominal tropopause level and  $\sim 420$  K and (2) distinct plumes with significantly elevated water vapor mixing ratios (*extrema*). To unequivocally distinguish the extrema, they are defined here as mixing ratios that are greater than  $3\sigma$  from the SEAC<sup>4</sup>RS mission-wide mean. It is a central objective of the following analysis to show that these extrema represent the characteristic signature of direct convective injection. Note that the majority of the extreme values observed during SEAC<sup>4</sup>RS were observed during plume encounters on the flight of 27 August 2013.

#### 2.4. SEAC<sup>4</sup>RS 27 August 2013 Plume Encounter

The 27 August 2013 flight provided key observational evidence wherein the ER-2 achieved all three of the objectives outlined above. The large-scale dynamical setting was characterized by a well-defined anticyclonic circulation in the UTLS common in the summer, i.e., the NAMA, which can increase the residence time of air parcels over CONUS for an average of 5 days [Sun and Huang, 2015; Koby, 2016]. A strong gradient in tropopause height in the proximity of the Rocky Mountains, i.e., low to the west and high to the east, marked the western edge of this circulation, and the center was positioned over the north-central Great Plains [Toon et al., 2016]. Additionally, real-time Next Generation Weather Radar (NEXRAD) Weather Surveillance Radar, 1988 Doppler (WSR-88D) reflectivity data revealed the locations of several recent deep convective storms over the U.S., many of which were energetic enough to penetrate the tropopause [Toon et al., 2016]. The data showed that the region extending from the Northern Great Plains to Southern Canada and eastward across the Great Lakes was impacted by a series of large convective storm systems over a period of several days, and forecast trajectory calculations were used to predict the storm outflow region and to direct flight planning. Accordingly, on 27 August 2013, the ER-2 headed north out of Houston, TX, to sample vertical gradients within the NAMA, as well as outflow from the recent storm systems.

#### 2.3. SEAC<sup>4</sup>RS Mission Overview

A central goal of NASA's SEAC<sup>4</sup>RS field mission, based out of Ellington Field in Houston, TX, during August and September of 2013, was to gain an improved understanding of how radiatively and chemically important atmospheric constituents are transported vertically through the atmospheric column, i.e., from the boundary layer through the lower stratosphere [Toon et al., 2016]. The unique capabilities of the high altitude NASA ER-2, which carried an array of in situ instrumentation for measuring water vapor, and other long-lived trace gases provided the means to (1) determine the depth of tropopause-penetrating storms, (2) examine the chemical impact of convective penetration into the stratosphere, and (3) probe the role of the large-scale circulation, i.e., the summertime, quasi-stationary North

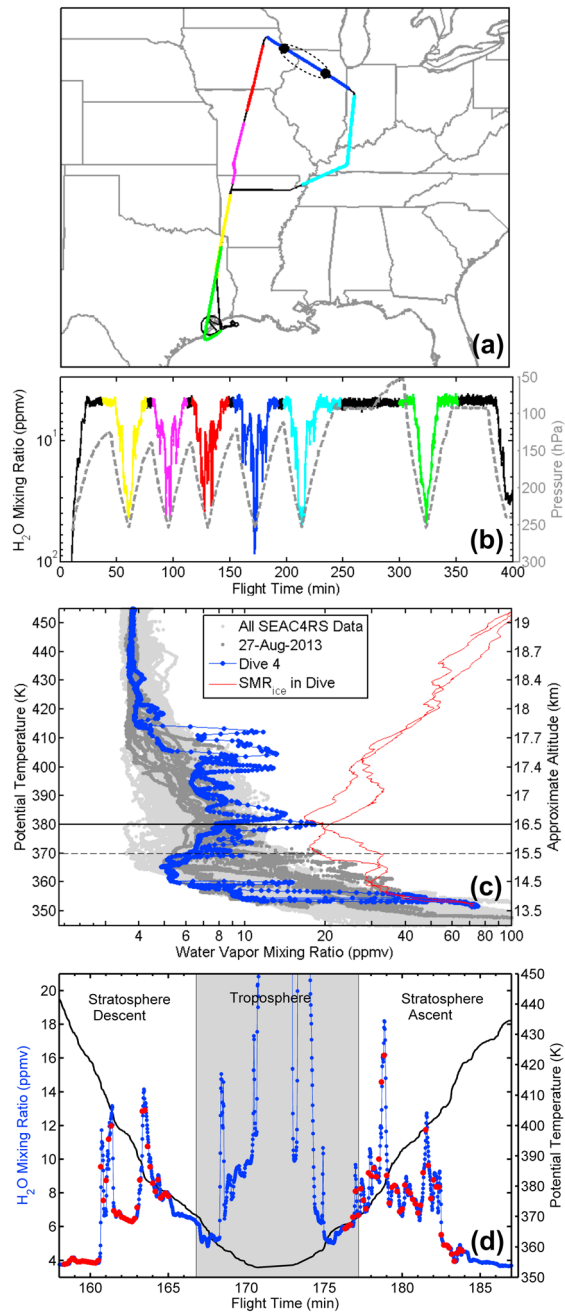


**Figure 3.** ER-2 flight track, vertical profiles and time series for the 27 August 2013 flight. (a) The flight track is color-coded by segment. Plume encounters on descent/ascent of Dive 4 (blue), which was executed just south of the Great Lakes, are indicated by the solid black circles. (b) Water vapor mixing ratio as measured by HWV and ambient pressure are plotted as a function of flight time. Note that the scales are inverted. The aircraft performed six vertical dives, color-coded to match the segments in Figure 3a. (c) Vertical profiles of water vapor mixing ratio as a function of potential temperature show the large enhancement sampled on Dive 4. The red lines (one for descent and one for ascent) are profiles of the simultaneous saturation mixing ratio with respect to ice ( $SMR_{ice}$ ). Note the logarithmic scale on the x axis. (d) Water vapor mixing ratio (blue) and potential temperature (black) for Dive 4 are plotted as a function of flight time. The red dots correspond to points along the flight track (10 s) that were used to initialize the back trajectory analysis (see section 3.2).

Figure 3a shows the ER-2 flight track for this day superimposed on a map of the U.S., and Figure 3b shows the corresponding time series of water vapor mixing ratio and ambient pressure (note the scales are inverted) for the 27 August 2013 flight. Six vertical sampling dives were executed along the flight track to probe the chemical composition of the UTLS within the NAMA [Toon *et al.*, 2016]. Moisture plumes were encountered in the overworld stratosphere on at least two of these descent/ascent vertical profiles. Figure 3c shows high-resolution water vapor data acquired by HWV (1 s) as a function of potential temperature during this flight. Dive 4 (blue dots) reveals a plume of significantly elevated water vapor present above both the local tropopause level and the 380 K surface and evident up to 415 K. This encounter, which occurred just south of the Great Lakes, registered the highest stratospheric water vapor enhancements of the mission, with mixing ratios reaching 18 ppmv, or 11 ppmv above a background of 7 ppmv at 380 K, and reaching 12 ppmv, or 8 ppmv above a background of 4 ppmv at 412 K.

Because the plume was sampled during a dive, we have precise information regarding its vertical extent and structure. The locations of the aircraft encounter with the plume on descent and ascent of Dive 4 are denoted by the two solid black dots on the map in Figure 3a. The plume extended from ~375 to 415 K (~115 to 85 hPa), corresponding to a depth of ~2 km (15.8 to 17.8 km), and there were two large magnitude water vapor excursions (or plume “lobes”), each with their own finer scale structure, which comprised the plume as a whole. These features are evident in both the descent and ascent profiles, though the features in the ascent profile are displaced vertically by about  $-5$  K in potential temperature. The repetition of the vertical

structure of the plume on descent and ascent, evident in the time series in Figure 3d, suggests that we sampled the same outflow plume on both legs of this dive. Due to the limitations of aircraft sampling, it is impossible to ascertain the full horizontal extent of the plume. Nonetheless, we infer that it extended at least from the aircraft encounter on descent at its western edge (42.58°N, 90.96°W, 19:40 UTC) to the aircraft reentry on ascent at its eastern edge (41.54°, 89.00°W, 20:00 UTC). This span is ~200 km primarily in the zonal direction. Despite limited information about its true meridional extent, if we assume a quadrilateral area constrained by the aircraft locations at intercept, we estimate that it covered an area of at least 20,000 km<sup>2</sup>.

### 3. Linking the Moisture Plume to Its Convective Source

To link the convectively sourced plume observed on 27 August 2013 to its source storm system, we employ several complementary data types. In order, these include (1) results from an OT detection algorithm that utilizes Geostationary Operational Environmental Satellite (GOES-13) infrared imagery to provide a record of tropopause-penetrating convection across North America; (2) calculations of isentropic back trajectories for air parcels initialized within the plume encounter along the 27 August 2013 aircraft flight track, which provide a spatial and temporal history of air parcel motion; (3) a summary of the local meteorological conditions at the time and location of the case study storm system highlighting several factors favoring convective penetration of the stratosphere; (4) a composite analysis of data from the ground-based NEXRAD WSR-88D precipitation radar network that provides a detailed 3-D history of the storm system; and (5) complementary visible and infrared images of the same storm system from the GOES-14 satellite operating in super rapid scan mode (1 min frequency) that show evidence for both overshooting tops and detraining above-anvil plumes. A discussion of each of these data types and analysis results is provided below.

#### 3.1. GOES-13 Overshooting Top Detections

In order to identify the storm system or systems that sourced the 27 August 2013 plume, it is necessary to have a comprehensive continental scale catalog of deep convection. For the SEAC<sup>4</sup>RS mission, infrared imagery acquired by the GOES-13 satellite (positioned at 75°W), which has an effective resolution of ~7 km and a 15 min scan rate, was input into an algorithm developed and tested for the purpose of identifying OTs, defined here as convective overshoots that penetrate the local tropopause level [Bedka, 2011; Bedka *et al.*, 2010, 2012]. The resulting OT product is ideally suited for identifying and locating deep convective storms—evident as clusters of OTs—capable of lofting water (predominantly in the condensed phase) into the stratosphere.

GOES-13 infrared brightness temperature data are used to detect cloud top temperature anomalies (cold pixels) within larger thunderstorm anvils. Because overshooting parcels are rising and cooling adiabatically, they can be colder than the surrounding anvil as well as the local lapse-rate tropopause, with the temperature difference indicative of both the strength of the convective updraft and the depth of penetration. Therefore, in the identification of OTs, two quantities are considered: the difference in temperature between OT candidates and the surrounding anvil cloud and the difference in temperature between OT candidates and the local tropopause as determined from Global Forecast System (GFS) Numerical Weather Prediction (NWP) model output. If the measured quantities show that an OT candidate is at least 6 K colder than the anvil, cooler than an adjusted tropopause temperature, and colder than 217.5 K, the OT is validated for the OT product [Bedka *et al.*, 2010]. These criteria in effect ensure that the final OT product consists of OTs that have exceeded not only the anvil level but also the tropopause.

Comparisons with higher resolution satellite-borne instruments, the Moderate Resolution Imaging Spectroradiometer (MODIS) and Visible Infrared Imaging Radiometer Suite (VIIRS), have shown that GOES-13 IR temperatures are biased warm. This is due to a combination of the sensor technology employed by GOES as well as the coarse spatial resolution of GOES relative to the other sensors [Griffin *et al.*, 2016]. This warm bias does not impact the determination of the OT-anvil criterion as it is the relative temperature difference that is the critical quantity. In this case, the temperature of the surrounding anvil is determined by averaging the temperature of all pixels with IR temperatures colder than 227.5 K that are 4 pixels from the coldest pixel in the region of the candidate OT. A 4-pixel radius is selected to ensure that the anvil regions being sampled are outside the range of the OT (typically 15 km maximum diameter). An adjustment,

however, is required for comparison with the local tropopause temperature. The native resolution of the GFS-NWP model used for the tropopause comparison is  $0.5^\circ \times 0.5^\circ \times 64$  hybrid sigma-pressure levels  $\times 6$  h [Sela, 2009], and the tropopause is determined using the World Meteorological Organization (WMO) lapse-rate definition [World Meteorological Organization (WMO), 1957], and then interpolated linearly in time to the OT pixels. For simultaneously sampled OTs, the requirement that the GOES-13 IR temperature be less than the GFS-NWP tropopause plus 5 K, to account for the GOES-13 bias, has been shown to be consistent with the requirement that the MODIS/VIIRS IR temperature be less than the GFS-NWP tropopause.

The absolute height of the verified OTs is subsequently determined from knowledge of three terms: the anvil height, the candidate OT-anvil temperature difference observed by GOES-13, and an assumed constant lapse rate derived from simultaneous MODIS-CloudSat OT overpasses that quantifies the rate at which OTs cool as they rise above the anvil ( $-\Delta T/\Delta z = 7.3$  K/km) [Griffin *et al.*, 2016]. The anvil cloud height is determined based upon a match between the anvil mean temperature and the GFS-NWP model temperature profile. The relationship between temperature and altitude within the UTLS is then used to convert the OT-anvil temperature difference to an absolute altitude.

Uncertainties in the OT height determination arise from the fact that GOES-13 temperatures likely emanate from an altitude  $\sim 1$  km below the physical cloud height that would be measured by more precise instrumentation, e.g., aircraft-borne and satellite-borne lidar [Sherwood *et al.*, 2004; Minnis *et al.*, 2008]. Additional uncertainties associated with the lapse rate determination may also lead to a systematic underestimation of the OT altitude above the anvil of  $\sim 1$  km. In total, these factors suggest that the estimated OT heights may be as much as 2 km too low. The net result is that the verified OTs are likely to have penetrated to higher altitudes, i.e., deeper into the stratosphere, than recorded in the SEAC<sup>4</sup>RS OT product. Because the primary function of the GOES-13 OT product in the present analysis is to identify convective storms characterized by frequent, deep, tropopause-penetrating events during the SEAC<sup>4</sup>RS period, it is not necessary to identify every single OT or to determine the exact OT height. Rather, the focus here is to identify prominent clusters of OTs that penetrated the local tropopause.

For SEAC<sup>4</sup>RS, every available GOES-East and GOES-West scan was processed for the full duration of the mission, even for the nonflight days, yielding a detailed and comprehensive data set of the location, timing, and depth of stratospheric penetration of convective storms over CONUS. The output files include the OT geospatial coordinates, time, overshooting intensity in degrees K—related to the temperature difference between the OT and the anvil—and the estimated maximum cloud height for each OT in meters.

### 3.2. Isentropic Back Trajectories and Candidate Storm Identification

Isentropic back trajectories (BTs), which represent the idealized motion of air parcels backward in time, are used to link the in situ observations of elevated water vapor to potential convective sources identified in the GOES OT data set. The trajectories are computed with the TRAJ3D trajectory model [Bowman, 1993; Bowman and Carrie, 2002], which uses a fourth-order Runge-Kutta scheme to solve the kinematic equations of motion with a 30 min time step. Winds are taken from the interim reanalysis of the European Centre for Medium-Range Weather Forecasts (ERA-I), which has a native resolution of  $\sim 0.7^\circ \times \sim 0.7^\circ \times 60$  vertical levels  $\times 6$  h ( $\sim 1$  km vertical resolution in the UTLS) [Dee *et al.*, 2011]. The ERA-I model grids have then been interpolated to isentropic surfaces at 350, 370, 395, 430, and 475 K, by the National Center for Atmospheric Research (NCAR), which makes the resulting files publicly available. Within TRAJ3D, the winds are interpolated to continuous parcel locations using linear interpolation in space and time. Trajectories are computed isentropically; that is, the diabatic heating rate,  $d\theta/dt$ , is assumed to be zero. The total diabatic heating rate in the lower stratosphere is small,  $<0.5$  K/d, so this is a valid approximation over a 10 day period. Furthermore, because the trajectory calculations are purely kinematic, no attempt is made to estimate mixing that occurs along the trajectories. Small clusters of parcels (discussed further below) are initialized at the aircraft longitude, latitude, and potential temperature at 10 s intervals along the flight track and integrated backward in time for 10 days. The TRAJ3D outputs for each parcel include Julian day, time of day in seconds, longitude, latitude, and altitude (potential temperature in K). In total, 23 initial locations were used within the descent segment of Dive 4 and 34 initial locations were used within the ascent segment, respectively.

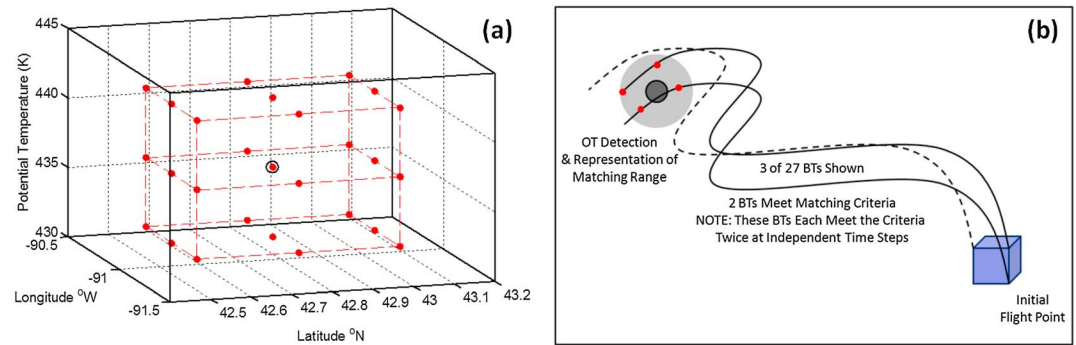


**Figure 4.** Representation of back trajectory initialization and match criteria. (a) To account for uncertainties in the trajectory calculations, a cluster of 27 BTs was initialized every 10 s along the flight track. The center of the cluster was located at the latitude, longitude, and potential temperature of the aircraft location (black circle), with the rest of the points spaced  $\pm 0.25^\circ$  and  $\pm 5$  K from the center (solid red circles). (b) BTs were calculated, and data output every hour for a 10 day period. An OT (dark gray circle) is flagged as a match if there is spatial and temporal coincidence between its match criteria envelop (light gray shaded area) and a point along a BT (wavy lines). This schematic shows that two (solid lines) of the three BTs shown fall within the match criteria envelope and one does not (dashed line). The matches are denoted by the solid red circles. In this example, each BT matches the specified OT at two time steps.

The temperature, pressure, and altitude along each BT were also calculated and output. Note that for isentropic trajectories, the pressure, temperature, and altitude of the parcel can change as long as potential temperature is kept constant. In addition to wind, the NCAR ERA-I product includes pressure ( $P$  (Pa)) and the Montgomery stream function ( $M$  (J/kg)) on potential temperature surfaces.  $P$  and  $M$  at each BT location and time were evaluated by linear interpolation. Temperature along the BTs was computed using  $T = \Theta \cdot \left(\frac{P}{P_0}\right)^\kappa$  in [K], with  $\Theta$  equal to potential temperature,  $P$  the interpolated pressure,  $P_0$  the reference pressure (equal to 101,325 Pa), and  $\kappa = R/c_p = 0.286$  for air.  $R$  represents the gas constant, and  $c_p$  is the specific heat capacity at constant pressure for dry air. The corresponding parcel geopotential height,  $Z$ , was computed from  $Z = (M - c_p \cdot T)/g$  in [m], with  $g$  equal to the gravitational acceleration of Earth. The geopotential height is nearly equivalent to the geometric height, only differing by 60 m at 20 km, due to the decrease in  $g$  with altitude [Andrews et al., 1987].

Uncertainties in the trajectories can arise from multiple sources including errors in the ERA-I winds caused by underlying observational or model errors; errors arising from the temporal and spatial resolutions of the reanalysis model; unresolved components in the reanalysis wind field, such as convection; and truncation error in the numerical scheme used to compute the trajectories. With a 30 min time step, the truncation error is small compared to the other error sources [Bowman et al., 2013]. Uncertainties in the analyzed wind direction are typically small except in areas of low wind velocity, and global root-mean-square errors in wind speeds for ERA-I are on the order of a few meters per second at the altitudes of interest [Dee et al., 2011]. A 1–2 m/s error in wind speed, for example, can lead to a maximum error in parcel position of  $\sim 100$  km (or  $1^\circ$ ) over the course of a day; however, trajectories in the lower stratosphere have typically demonstrated better agreement than this with atmospheric features observed by aircraft and satellites for time scales up to a week [Schoeberl et al., 1993; Bowman, 1993; Bowman et al., 2007]. Strong vertical shear in the horizontal wind increases the sensitivity of the computed trajectory to initial conditions, and additional uncertainty can arise from the 6 h synoptic reanalysis frequency. Finally, in the presence of convection, the horizontal winds will have larger errors than normal due to the fact that storm-scale convergence and divergence are not resolved in the reanalysis model.

To help account for these uncertainties in the trajectory calculations, a cluster of 27 parcels arranged in a  $3 \times 3 \times 3$  grid ( $\pm 0.25^\circ$  in latitude, by  $\pm 0.25^\circ$  in longitude, by  $\pm 5$  K in potential temperature, which is roughly equivalent to 200 m in altitude) was initialized every 10 s along the aircraft track. The technique of using a cluster instead of a single trajectory is similar to that employed by Sayres et al. [2010]. Whereas a single trajectory offers a binary solution that can miss the impact of some convective systems due to the aforementioned uncertainties, the cluster approach allows for a more lenient determination of convective influence. Schematics illustrating the initialization of a cluster and its associated BTs are shown in Figures 4a and 4b, respectively.

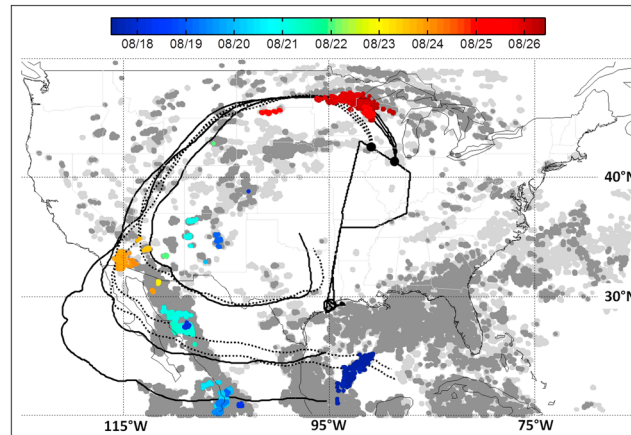


**Figure 5.** OTs 10 days prior to the plume encounter and BTs initialized within the plume encounter. All OTs (light gray dots) for 10 days prior to the plume encounter are shown on a map of the continental U.S. OTs with cloud tops exceeding 16 km altitude (dark gray dots) and OTs that meet the coincidence criteria for BTs initialized within the 27 August 2013 plume encounter (colored dots) are highlighted. The color-coding corresponds to day of month (MM/DD). Also shown is the ER-2 flight track with selected 10 day BTs (curved solid and dashed black lines) initiated at the time and location of the plume intercept on descent/ascent of Dive 4 (solid black circles).

### 3.3. Identifying the Source Storm for the 27 August 2013 Outflow Plume

To identify the storm system that was the most likely source for the high water vapor data observed on Dive 4 of the 27 August 2013 flight, we designate an OT as a candidate when there is temporal and spatial coincidence between it and a point along a BT initialized within the plume encounter. To meet the criteria for coincidence, a BT must pass within 1° in latitude and longitude and within ±2 h of the OT occurrence. The 1° criterion was selected to be consistent with the integrated 1 day uncertainty in position discussed above, and the ±2 h window accounts for the 1 h resolution of the trajectory output as well as uncertainties in the trajectory calculations and underlying reanalysis wind

speeds. We also apply an altitude filter. We use the estimated OT altitude from the GOES analysis to select for those OTs that either exceed the altitude of the BT at the matching location and time or are within 0.5 km of the BT altitude, i.e., if  $BT_{altitude} - OT_{altitude} < 0.5$  km. Finally, the cluster of 27 trajectories initialized around each flight point allows us to capture the sensitivity of the trajectory analysis to small changes in initial conditions. We consider an OT to be a more likely candidate when a greater fraction of the BT cluster meets the criteria listed above. The schematic in Figure 4b illustrates a match between an OT and a point along a BT initiated within the plume.

Figure 5 shows the geographic locations of all GOES OT detections over North America for 10 days prior to the aircraft encounter (light gray dots), those with cloud top altitudes greater than the local tropopause level at 16 km (dark gray dots), and those that met the spatial and temporal coincidence criteria, from the OT-BT analysis (colored dots). In total, there were  $27 \times N$  trajectory runs, where  $N$  is the number of points initialized within the aircraft plume encounter on descent and ascent ( $N = 57$ ). The colored dots highlight every OT that met the spatial and temporal match criteria for at least one of these  $27 \times N$  trajectories. We highlight those OTs that exceeded 16 km because they represent the OTs most likely to lead to hydration of the overworld stratosphere. Of the OTs that meet the spatial and temporal matching criteria, ~95% have maximum altitudes greater than 16 km.

The data show that during the 10 day period prior to the 27 August 2013 flight, there were three primary areas of deep convective activity: (1) the region over the Sierra Madre in Mexico and the southwestern U.S., which is typically referred to as NAM convection; (2) the region off the southeast coast of the United States and over the Gulf of Mexico; and (3) the region extending from the Great Plains to Southern Canada and eastward across the Great Lakes. Limiting our selection to those OTs that meet the match criteria (colored dots) causes the distribution to contract to a few discrete storm systems that occurred between 10 h and up to 9 days prior to flight. The most recent of these is the storm system that occurred over Minnesota and Wisconsin between 26 August 2013 21:00 UTC and 27 August 2013 12:00 UTC (hereafter MN-WI). In the following section, we demonstrate that this system is the most likely source for the high water vapor values in the plume sampled by the ER-2.

Also plotted in Figure 5 are six trajectories, three from the cluster of 27 BTs initialized within the higher-altitude plume segment encountered on Dive 4 descent (dotted lines) and another three that were initialized within the higher-altitude segment on ascent (solid lines). These plume encounters on descent/ascent have similar

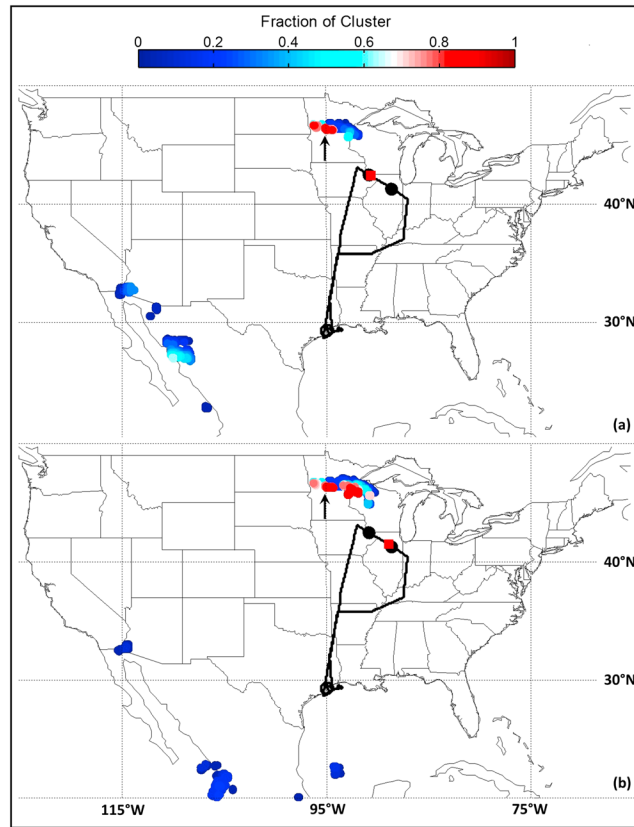


**Figure 6.** Candidate OTs for individual plume points. (a) The location of all OTs that meet the match criteria for a single point (red square) within the plume encounter on descent of Dive 4 are shown. The color coding corresponds to the fraction of the cluster of 27 BTs that meet the match criteria, with red circles indicating  $>0.8$  match. (b) Same as Figure 6a, but for a corresponding point (red square) within the plume encounter on ascent of Dive 4. The black arrows specify the location of the storm snapshot captured in the NEXRAD maps shown in Figure 8.

the three pass in the vicinity of storms at the Arizona/California border, over the west coast of Mexico, and over the Gulf of Mexico. If the time criteria between these BTs and the OTs are met, there is some likelihood that each one of these storms could have contributed to the moisture observed at this point in the plume. The most likely storm to have sourced the observed plume, however, is the most recent one, i.e., the MN-WI storm complex because this storm shows the greatest coherence of trajectories for points initialized at comparable altitudes during both the descent and ascent encounters.

Figures 6a and 6b show only those OTs that meet the spatial and temporal match criteria for BTs initialized when the aircraft encountered the peak of the lower-altitude plume segment on both descent (19:42:34 UTC) and ascent (19:58:04 UTC) of Dive 4, respectively. The color coding in these figures corresponds to the fraction of each BT cluster that satisfies the selection criteria, with the red colors indicating a higher fraction ( $>80\%$ ) and thus a greater likelihood that an individual OT was a candidate for the observed water vapor enhancement. These two figures broadly represent the results for 7 points that encompass the lower-altitude lobe of the plume on descent and 6 points that encompass the corresponding lobe on ascent. In every case, the storm system that developed and matured over Minnesota and Wisconsin (MN-WI) is the dominant candidate. Though we cannot rule out potential influence from storms that occurred further back in time, e.g., the clusters of OTs located over southwestern Arizona and along the west coast of Mexico roughly 3–7 days prior to the plume encounter, two features of the analysis lead us to conclude that the MN-WI storm system is the primary source. (1) A majority of unique OTs (73%) in the cluster associated with the MN-WI storm system meet the match criteria for points initialized within the plume encounter. (2) This is the only

magnitude water vapor ( $>10$  ppmv) and occurred at similar potential temperatures ( $\sim 400\text{--}410$  K). Some, but not all, of the colored OTs meet the match criteria for the six trajectories shown. The trajectories illustrate the flow pattern associated with the NAMA circulation, demonstrating that these air parcels were circulating over CONUS for at least 3, and in some cases, more than 10 days prior to the aircraft plume encounter. They also demonstrate the sensitivity of the calculations to subtle differences in initial conditions. In this case, the latitude and longitude of the three trajectories in each set are identical, but the potential temperatures differ by  $\pm 5$  K ( $\sim 200$  m) about the center position located along the aircraft flight track. Both sets of trajectories show the divergence with time that results from wind shear in the lower stratosphere. Finally, the trajectories suggest that the air parcels may have been influenced by more than one tropopause-penetrating convective storm system during their confinement over North America.

storm system that matches the plume encounter in its entirety, i.e., it is the only cluster with OTs that match points initialized within both the upper and lower lobes of the plume during both the descent and ascent encounters. (3) For nearly every point initialized within the plume, the BT analysis favors OTs within the MN-WI storm system.

### 3.4. Meteorological Context

The meteorological conditions over the U.S. near the end of August 2013 were ideal for generating the strong tropopause-penetrating MN-WI storm system that originated on the western border of Minnesota around 27 August 2013 00:00 UTC and moved east across Wisconsin over the following five or more hours. Similar to a long-term climatology for the region, the prevailing near surface circulation pattern at 850 hPa on 26 August 2013 was characterized by a northward flow carrying warm, moist air originating off the Gulf of Mexico, along the eastern edge of the Rocky Mountains and across the northern Great Plains. This flow converged with a weaker but predominantly eastward flow in the vicinity of the Canadian border and then turned east in the vicinity of the Great Lakes with daily variations in its northerly extent. The flow at higher levels, e.g., 500 hPa, for this period, originated with air coming off the Gulf of California and Tropical Pacific. This air was carried north-northeast over the Rocky Mountains and then eastward over the northern Great Plains as a part of the NAMA circulation. The combination of (1) a well-defined low-level jet between 850 and 900 hPa supplying moist air at low levels and (2) colder air aloft was ideal for the development of deep convection as it led to steep tropospheric lapse rates and a corresponding decrease in atmospheric stability [e.g., Brooks *et al.*, 2003; Zipser *et al.*, 2006].

Convective available potential energy (CAPE), a measure of the maximum kinetic energy available to an ascending parcel (i.e., positive buoyancy), provides a means of predicting the intensity and updraft strength of thunderstorms [e.g., Brooks *et al.*, 2003; Holton, 2004; Trapp *et al.*, 2009]. Observed values of CAPE in thunderstorm environments often exceed 1000 J/kg, with values greater than 4000 J/kg indicative of extreme instability. Atmospheric soundings out of Minneapolis, MN, during 24 h prior to the development of the MN-WI storm, showed large CAPE values ranging from approximately 2000 to 4000 (J/kg), confirming that conditions were favorable for powerful storms.

### 3.5. NEXRAD Analysis of Storm Evolution and Stratospheric Penetration

The extensive coverage of the NEXRAD WSR-88D network throughout CONUS [Crum and Alberty, 1993], in combination with the development of sophisticated data processing algorithms, has yielded a powerful high spatial and temporal resolution product for three-dimensional studies of convection [Homeyer, 2014; Homeyer and Kumjian, 2015]. Individual radar volume scans from multiple radars are merged into high-resolution three-dimensional composites every 5 min on a regular  $0.02^\circ$  ( $\sim 2$  km) longitude-latitude grid with 1 km resolution in the vertical. We use this processed NEXRAD data to provide a detailed account of the structure and time evolution of the MN-WI storm system identified by the OT and BT analysis shown in Figure 6.

We employ one of several available radar variables: the radar reflectivity at horizontal polarization,  $Z_H$ , typically expressed in units of decibels of the radar reflectivity factor  $Z$  (dBZ).  $Z$  is a function of both the number of cloud particles per unit volume and cloud particle size, with its value proportional to the sixth moment of particle diameter ( $D^6$ ) assuming spherical particles. The NEXRAD WSR-88D radars are capable of reliably detecting cloud particles producing echoes (nonzero values of  $Z_H$ ) as small as  $-42$  dBZ and as large as 75 dBZ, with the smaller reflectivities detectable at ranges nearer to the radar location. Deep convection is typically characterized by a column-maximum  $Z_H$  in excess of 45 dBZ, and the echo top (or storm top) altitude is the highest level in each radar composite column that is equal to or greater than a specified threshold. The echo top altitudes shown here are for a radar reflectivity threshold of 15 dBZ. Uncertainties in the echo top determination, which have been evaluated via comparison with higher-resolution vertically pointing radars, are between 500 m and 1 km depending on coverage within the NEXRAD network [Homeyer, 2014].

Figure 7a shows a 15 h history of the maximum echo top height, expressed in both altitude and corresponding potential temperature, determined at each location for the period from 26 August 2013 21:00 UTC to 27 August 2013 12:00 UTC using the 5 min composite data set. This window encompasses the full lifetime of the MN-WI storm system. Due to the reduced density of the NEXRAD network in Northern Minnesota, the vertical sampling is limited, and there is larger uncertainty in the echo top determination in this region ( $\sim 1$  km). Nonetheless, it is clear that the candidate storm system penetrated both the local tropopause level and

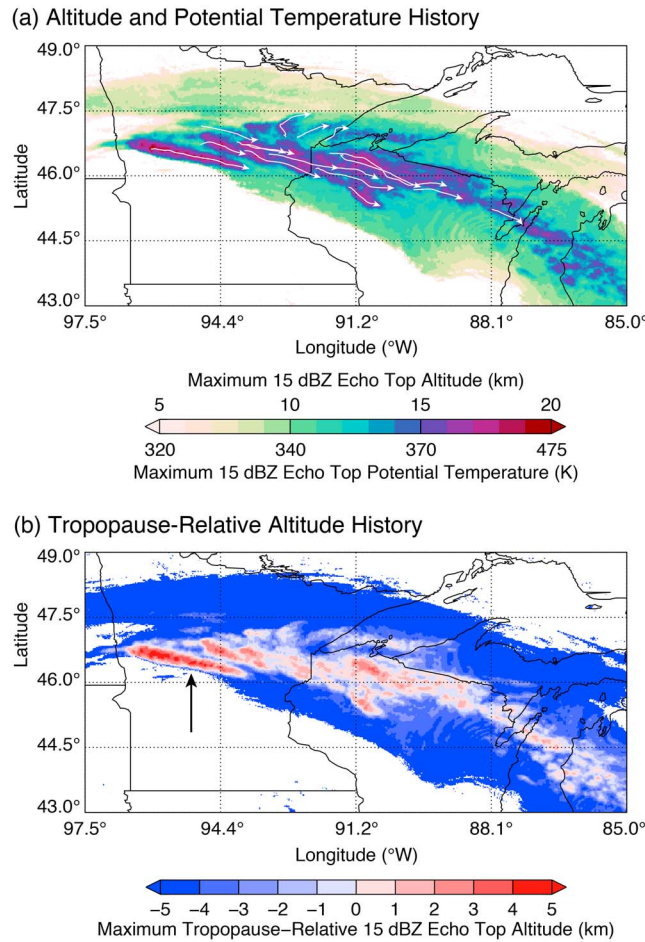


**Figure 7.** Maps showing the 15 h evolution of stratospheric penetration depth for the candidate storm system using NEXRAD data. (a) The maximum storm top altitude recorded at each location between 21:00 UTC on 26 August 2013 and 12:00 UTC on 27 August 2013 from 5 min NEXRAD WSR-88D radar composites, expressed in both altitude and the corresponding potential temperature. This interval encompasses the full lifecycle of the MN-WI storm system that was identified in the GOES OT and BT analysis. The color-coding corresponds to the storm top altitude (the 15 dBZ radar reflectivity echo top), with the dark blue and purple colors indicating storm tops reaching altitudes >15 km (>370 K). Several individual long-duration (>2 h) storm tracks are evident within the larger complex (white arrows). (b) The difference between the maximum storm top altitude and the altitude of the local tropopause from ERA-I (~16 km) is shown for the same period. The pink and red colors denote penetration into the stratosphere. The black arrow specifies the location of the storm snapshot captured in NEXRAD data that is shown in Figure 8.

central Minnesota. The NEXRAD record of the location and time of tropopause-penetrating storm tops also provides independent verification of the GOES-13 OT product.

The NEXRAD composite data show that a considerable area of the overworld stratosphere was exposed to convective overshoots and turbulent mixing leading to the potential for large enhancements in stratospheric water vapor concentrations. The data set also provides the means to objectively quantify the area impacted by tropopause-penetrating convection over the lifetime of the MN-WI storm system. The area of storm tops exceeding the local tropopause level was determined from 5 min radar volumes over the domain of the maps in Figure 7. The cumulative sum of the 5 min data yields a total area impacted of 113,620 km<sup>2</sup>, and the total area impacted without counting every 5 min occurrence independently yields a value of 36,786 km<sup>2</sup>. The

the overworld stratosphere. The purple colors represent storm tops at or exceeding 17 km (~400 K), and in the most intense regions, penetrations regularly reached or exceeded 18 km (~425 K). Furthermore, the NEXRAD 15 h history shows that there were at least five individual long-lived (>2 h) storms present within the larger system. These individual storms, evident as thin wavy white lines, were tracked utilizing the objective storm-tracking method described by Homeyer *et al.* [2017]. Each one had echoes extending well above the tropopause level during its lifetime.

Figure 7b shows the same data with the maximum storm top altitude referenced to the local tropopause. The tropopause used in conjunction with the NEXRAD data is derived by applying the WMO lapse-rate definition [WMO, 1957] to ERA-I output on model levels. Tropopause altitudes are then interpolated linearly in space and time to the higher resolution radar grid for comparison. The agreement between tropopause altitudes computed from ERA-I and radiosondes is typically within ~500 m [Solomon *et al.*, 2016; Homeyer *et al.*, 2017]. The fact that the MN-WI storm system penetrated the local tropopause level frequently over the course of its lifetime is evident. The pink to red colors indicate regions where the radar observed storm tops at altitudes greater than the local lapse-rate tropopause. The depth of stratospheric penetration was as much as 4–5 km, and the strongest (deepest) storm was located farthest to the west over

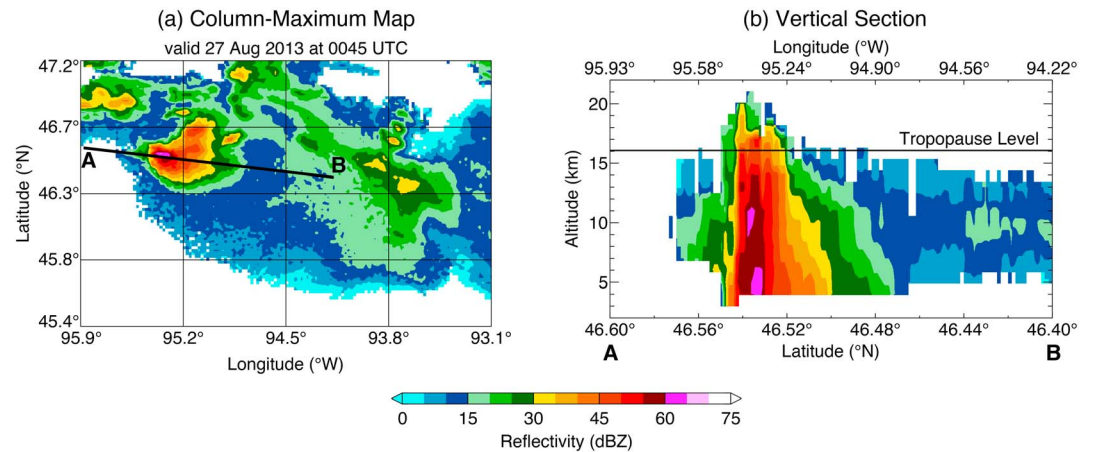


**Figure 8.** High-resolution storm map and 2-D cross section showing 4–5 km penetration into the stratosphere. (a) This map shows column-maximum radar reflectivity at a time of strong tropopause-penetrating convection (00:45 UTC on 27 August 2013) from composite NEXRAD observations. (b) A vertical cross section along the line labeled “A-B” in Figure 8a highlights the depth of penetration above the local tropopause (as determined using 00:00 UTC radiosonde observations from nearby Minneapolis, Minnesota). The reflectivity data reveal that significant condensate was carried to altitudes  $>4$  km above the tropopause level.

difference in these estimates arises from the fact that many locations along the storm tracks experience multiple overshoots. Though the magnitude of the cumulative area estimate depends in part on the motion of the storm relative to the temporal resolution of the radar product, it is clear that many regions were subject to repeated or sustained tropopause-penetrating convection.

The NEXRAD data also reveal what is occurring at high spatial and temporal resolutions. Figure 8a shows a map of column-maximum  $Z_H$  over central Minnesota for a particularly severe period in the development of the deepest storm at 00:45 UTC on 27 August 2013. A 2-D vertical transect along the line “A-B” in Figure 8a is shown in Figure 8b. This figure reveals the depth of penetration of convection above the local tropopause level (4–5 km), with the high  $Z_H$  (values  $\geq 30$  dBZ) indicating that significant condensate was carried well into the overworld stratosphere. Note that this image captures a single moment of the hours-long lifetime of just one of the storm tracks evident in Figure 7a.

### 3.6. GOES-14 Images Showing Stratospheric Penetration and Plume Formation

Visible and infrared data from the GOES-14 satellite provide further evidence of convective penetration into the stratosphere during this particularly intense interval of the MN-WI storm system. Both the position of the satellite and its scan mode were well suited to probe the detailed structure and evolution of the storm. GOES-14, which has an effective resolution of 6.4 km in the IR and 1.6 km in the visible, is positioned at 105°W and at this time was operating in “super rapid scan mode” [Schmit *et al.*, 2013]. In this mode, images are collected every minute with occasional gaps of up to 4 min.

GOES-14 observations in the visible show the locations of OT peaks and the shadows they cast on the surrounding anvil. Shadow length and knowledge of the image time/day can then be used to derive the above-anvil penetration height following the method described in Bedka *et al.* [2015]. Figure 9a shows a visible image captured by GOES-14 at 00:41 UTC on 27 August 2013, and Figure 9b records the evolution of estimated OT depth over the next 6 min. This time period is coincident with the NEXRAD radar reflectivity data shown in Figure 8. Long shadow slant paths at dusk make the determination of tower altitudes more difficult and considerably less accurate, and no height estimates were available after 00:46 UTC. However, for the 6 min analyzed here, the above-anvil OT penetration height grew from 2.16 km around 00:40 to 2.83 km by 00:46, with an error estimate of  $\sim 0.25$  km due to uncertainties in the determination of the shadow length and geometry. A comparison of the temperature of the anvil dome in the immediate vicinity of the OT (208 K) with the 00:00 UTC Minneapolis, MN, temperature sounding yields an anvil height of  $17.5 \pm 0.2$  km, which is consistent with the NEXRAD radar-reflectivity cross-section data shown in Figure 8b. Thus, with a shadow-derived above-anvil OT penetration height of  $\sim 3$  km, we estimate that the OT reached a max altitude of  $\sim 20$  km, or  $\sim 4$  km above the local tropopause (16 km), confirming the NEXRAD peak echo top at 00:45 UTC.

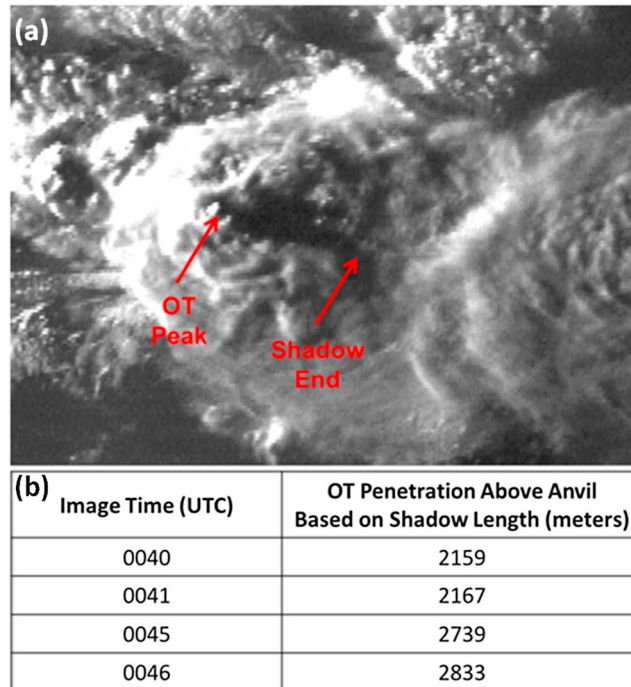


**Figure 9.** GOES-14 visible imagery showing OT height above anvil. (a) This image, recorded by the GOES-14 satellite during an intense period in the development of the case study storm system (00:41 UTC on 27 August 2013), highlights a single OT and the shadow it casts on the surrounding anvil cloud below. The above-anvil height of the OT can be determined from the measured shadow length in combination with time/day and geometry. GOES-14 was acquiring images every minute during this period. (b) The evolution of this OT over a 6 min interval. By 00:46 UTC the OT had penetrated to a height nearly 3 km above the anvil.

GOES-14 visible imagery also provides direct evidence for the existence of cirrus plumes that have detrained away from OTs at heights above the anvil [Setvák et al., 2013; Bedka et al., 2015; Homeyer et al., 2017]. Plumes of condensate, directly connected to OT locations, are evident in consecutive super rapid scan images for this intense period of the MN-WI storm system. The altered texture and shadowing associated with these plumes provides evidence that they are present above the level of the anvil. The image in Figure 10a, acquired at 00:11 UTC on 27 August 2013, reveals two active cirrus plumes (green ovals). For these cirrus plumes, the imagery shows material being ejected from OTs on multiple successive images. A long-duration animation of super rapid scan imagery from GOES-14 is provided as supporting information to show the evolution of OTs and above-anvil plumes during this period. Recently decayed OTs and detrained plumes (yellow ovals) as well as older, diffuse plumes from decayed OTs (dashed yellow ovals) are also evident in this visible image.

In contrast to actively rising OTs (cyan circles) that have colder tops than the surrounding anvil and tropopause, material ejected from OTs that has recently irreversibly mixed with the surrounding stratosphere (yellow ovals) will radiate at warmer temperatures than the anvil and tropopause. Both these cold and warm anomalies are evident in the infrared image shown in Figure 10b. In this image, the anvil associated with the storm cell on the right is predominantly composed of black pixels signifying a temperature of ~203 K (16 km, 380 K potential temperature), which is right at the level of the local lapse rate tropopause. The pixels in the central rising OT are purple, indicative of a minimum temperature of ~197 K or ~6 K colder than the anvil. Three other rising OTs (cyan circles) are also evident, two at the northeastern edge of the main cell and one in the maturing storm cell on the left. This is the OT examined in Figure 9 at a time ~30 min earlier in its development. In addition, there are two above-anvil regions that are radiating at warmer temperatures (yellow ovals). Both regions are composed of red pixels (~208 K, 17.5 km, 420 K potential temperature) and are surrounded by the black pixels of the colder anvil. These regions are approximately +5 K warmer than the anvil, which is equivalent to an above-anvil height of ~1.5 km. Similar warm anomalies, indicative of above-anvil plumes and detrainment, are evident throughout much of the lifetime of the MN-WI storm complex.

In summary, the GOES-13 OT detections in combination with the processed NEXRAD data, and GOES-14 imagery, considered within the regional scale meteorological context, all indicate that deep, tropopause-penetrating convection occurred frequently during the MN-WI storm system on 27 August 2013. The back trajectory analysis shows that this storm system was the most probable source for the water vapor plume observed by the ER-2 later that day. The plume represents the integrated effect of multiple OT events. Indeed, the GOES-13 product identifies 1821 unique OTs in the domain of the NEXRAD maps for the 15 h period encompassing the lifetime of this storm system. Together, the radar data and satellite visible and infrared

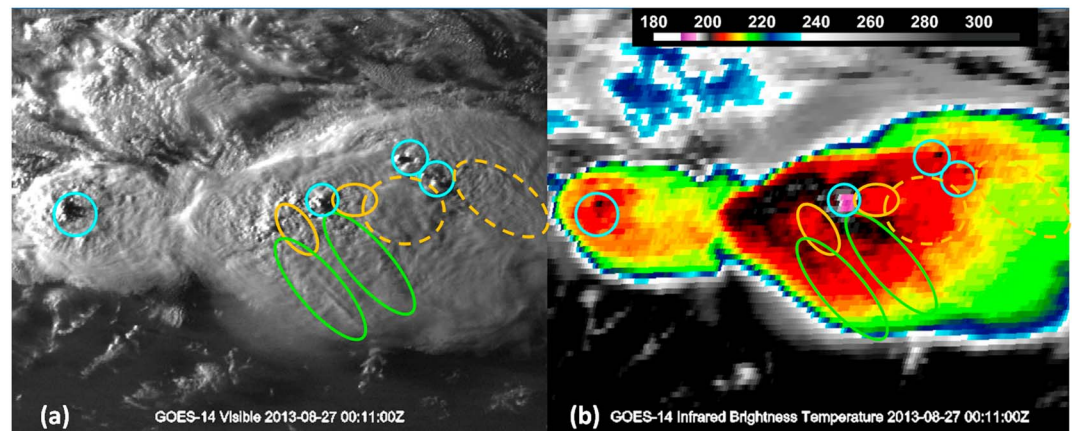


**Figure 10.** GOES-14 visible and infrared imagery of active and decayed plumes in the stratosphere. (a) Visible image acquired at 00:11 UTC on 27 August 2013 showing active plumes (green ovals) of condensate ejected from active OT regions. These cirrus plumes were evident on multiple successive images. (See also animation in the supporting information.) Also evident are diffuse plumes from decayed OTs (dashed yellow ovals), and actively rising OTs (cyan circles). The OT at the far left of the image is the one featured in Figure 9 at an earlier stage in its development. (b) The corresponding image in the infrared. Actively rising OTs are evident as colder pixels above the warmer anvil below. Plume material that has recently mixed with the surrounding stratosphere is evident as warmer red pixels (yellow ovals) above the comparatively cooler anvil.

imagery illustrate the processes of OT injection, mixing and detrainment of convectively lofted air and ice that leads to the irreversible transport of water into the stratosphere.

#### 4. Convection on the Broader Scale

For convection to irreversibly moisten the stratosphere, the storm systems must be powerful enough to penetrate the local tropopause and deposit ice directly into the subsaturated stratosphere where it can rapidly sublimate. There are several indications that North America, and the central U.S. in particular, is subject to a greater frequency of summertime, tropopause-penetrating convective storm systems than other regions at similar latitudes. Global distributions of deep convection show a high frequency of events over North America, in particular, over the Great Plains states of the U.S., with some events extending as far as 50°N [Laing and Fritsch, 1997; Doswell and Bosart, 2001; Brooks *et al.*, 2003; Zipser *et al.*, 2006; Liu and Liu, 2016]. No other region at comparable latitudes exhibits such a high frequency of extreme convective storm systems. Furthermore, because the altitude of the 380 K potential temperature surface decreases with latitude, deep convective storms, *i.e.*, those reaching or exceeding 16 km, are more likely to penetrate into the overworld at higher latitudes.

Climatological studies of convection focusing on CONUS, made possible by the development of the NEXRAD 3-D, gridded, composite radar reflectivity data set, show that tropopause-penetrating convection over this region has both a strong annual cycle and a characteristic geographic distribution [Solomon *et al.*, 2016]. Solomon *et al.* [2016] evaluated maximum storm-top altitudes at 3 h intervals for 1 year (2004) of composited NEXRAD data and determined the frequency, magnitude, and location of tropopause-penetrating storms by comparison with the lapse-rate tropopause determined from ERA-I. They found that tropopause-penetrating convection is most common in the north-central part of the U.S. (the Great Plains) and that there is a pronounced seasonal cycle, with the majority of overshooting systems occurring between March and August.

Ongoing investigations of the NEXRAD data have expanded the analysis to examine tropopause-penetrating convection over the U.S. for the months of March to August at 1 h intervals over 10 years (2004–2013) (J. W. Cooney, private communication, 2017). The study domain extended from 69°W to 115°W longitude and 25°N to 49°N latitude. As in Solomon *et al.* [2016], the geographic distribution of tropopause-penetrating storms was found to favor the central U.S., with the very deepest storms (absolute altitude) occurring more frequently in June, July, and August. Though there is significant interannual variability in the number of overshoots detected, there are on average ~46,000 overshooting convective updrafts for the months March

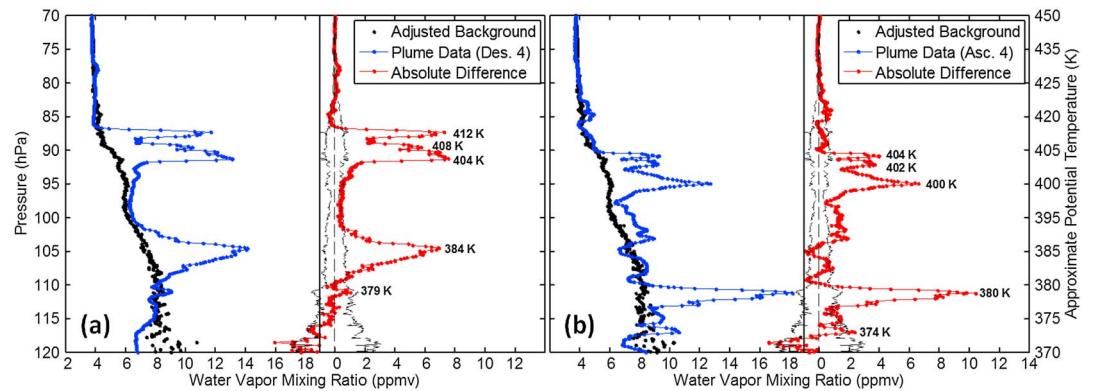


**Figure 11.** Vertical profiles of water vapor mixing ratio for Dive 4 of the 27 August 2013 flight. (a) The calculated unperturbed background profile (black) and 1 s measurements from within the plume (blue) encountered on descent of Dive 4 are plotted as a function of pressure. The absolute difference (red) between these two profiles is also shown. Above and below the plume regions, the difference is within one standard deviation of zero (thin black dashed lines). (b) Same as in Figure 11a, but for Dive 4 ascent. Potential temperatures for individual high water vapor extrema within the larger plume structure are identified for both descent and ascent. The approximate potential temperature coordinate is indicated on the right-hand vertical axis.

through August or ~250 per day that reach or exceed 1 km above the local tropopause level over the analysis region. It is estimated that approximately 50% (or ~125 per day) of these will surpass the 380 K potential temperature level and reach the overworld. While convective penetration is a necessary but not sufficient condition for hydration [e.g., *Homeyer et al.*, 2017], deep, tropopause-penetrating storms constitute a potentially important source for stratospheric water vapor over the U.S. in summer. Furthermore, the confinement of air parcels within the NAMA may be the effect of multiple storms over approximately week-long intervals.

In the following sections we calculate the net contribution of the MN-WI storm system to the water vapor budget in the overworld stratosphere, and then reexamine it within the broader context informed by the NEXRAD climatology of convection summarized above, in addition to aircraft and MLS satellite climatologies of convectively sourced extreme water vapor excursions over CONUS.

#### 4.1. Estimated Contribution of the MN-WI Storm to Stratospheric Humidity Over the U.S.

We estimate the convective contribution from the MN-WI storm system by integrating the difference between the profiles that sampled the plume on Dive 4 and an inferred unperturbed background profile. The multiple vertical sampling dives executed during the 27 August 2013 flight provide the data to establish a reliable background. An initial profile was determined by calculating the mean mixing ratio in each 0.1 hPa bin from 150 hPa to 60 hPa. Because the water vapor extrema skew this simple mean profile, we calculate a more robust bin-average profile by excluding all data greater than one standard deviation from the simple mean. This adjusted bin-average profile is then extrapolated to match the dimensions of the original 1 s water vapor data set. Figures 11a and 11b show the adjusted mean background profile (black), the measured values (blue), and the absolute difference between the two (red) as a function of pressure, for Dive 4 descent and ascent, respectively. The approximate potential temperature is shown on the right-hand vertical axis, and the potential temperatures of individual water vapor extrema within the larger plume structure are identified for both the descent and ascent profiles. In the regions immediately above and below the plume encounter, the measurements return to the nominal background value, with most of the data falling within the envelope of one standard deviation from the mean. Two features mentioned in section 2.4 stand out in this figure: (1) the distinct layering of the plume encounter, with peak values in each layer roughly double the background, and (2) the similarity in the vertical structure between sampling on descent and ascent.

In order to quantify the convective contribution, we begin by calculating the fractional change in column integrated water vapor for each vertical profile during the flight. To do this, we sum over the absolute difference between each of the measured profiles and the adjusted mean background profile from 115 hPa to 70 hPa and then divide by the corresponding sum over the background profile. The results for every dive descent and ascent, expressed as a percentage change in humidity over the specified pressure range, are plotted

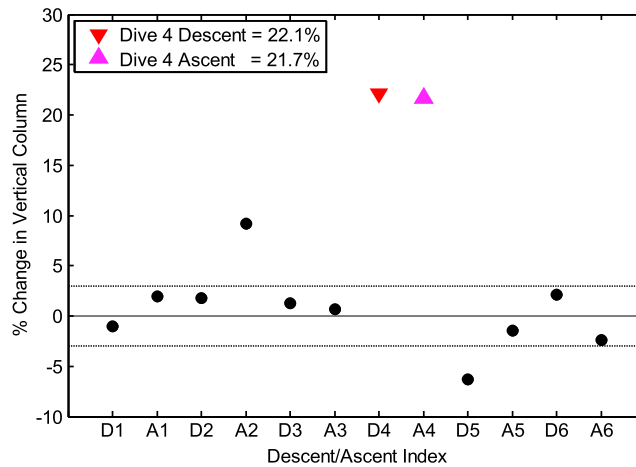


**Figure 12.** Percentage difference in integrated column water vapor evaluated for every descent/ascent profile of the 27 August 2013 flight. The vertical range considered is from 115 hPa to 70 hPa. The indices correspond to descent (D) and ascent (A) of each vertical sampling dive (#) (see Figure 3a).

in Figure 12. For eight of the 12 vertical profiles, the column integrated percentage differences are within  $\pm 3\%$  of zero. These profiles are indistinguishable, in an integrated sense, from the estimated unperturbed background. There may be positive and negative excursions over the vertical range, but in the net, they cancel. Four of the profiles, however, show significant deviations, with the descent and ascent of Dive 4 exhibiting the largest perturbations, 22.1% and 21.7%, respectively. The fact that most of the vertical samples yield near-zero results lends credibility to the estimated background profile for this flight day. Furthermore, the agreement in the column integrated

percentage change on both descent and ascent of Dive 4 provides quantitative validation that the same out-flow plume extended over this geographic region.

To calculate the total mass of additional water vapor in the overworld stratosphere associated with this plume, it is necessary to estimate the plume area. As stated in section 2.4, we had limited information about the full horizontal extent of the plume, but using the locations of the plume intercept, which were nearly equivalent at 70 hPa and 115 hPa, we estimate the area impacted to be 20,000 km<sup>2</sup> over this pressure range. This estimate constitutes a rational lower bound.

Solomon *et al.* [2016] show that there is a rapid decrease in overshooting volume with altitude above the tropopause, which results from the fact that the number of overshooting events declines exponentially with altitude. It is probable therefore that the area at the lower altitude/higher pressure levels is substantially larger than what was observed by the aircraft. Using the data from Solomon *et al.* [2016], we derived a simple exponential equation to describe how the plume area decreases with pressure above the tropopause. Given the observational constraint of 20,000 km<sup>2</sup> at 80 hPa, we estimate the plume area at 115 hPa (near the tropopause level) to be  $\sim 100,000$  km<sup>2</sup>. This more sophisticated determination of the plume area, which accounts for the change as a function of altitude, provides a reasonable upper bound for our calculations, and is consistent with the independent estimate obtained from the NEXRAD 5 min composite data described above, 113,620 km<sup>2</sup>.

Using these area estimates, we convert the absolute difference (Figure 11a and 11b) over the vertical column from 115 hPa to 70 hPa to an integrated mass using the following equation:

$$[\text{Mass H}_2\text{O Added to Column}]_{115-70 \text{ hPa}} = \int_{115 \text{ hPa}}^{70 \text{ hPa}} \text{Area}(P) \cdot \left(\frac{1}{g}\right) \cdot (P) \cdot \Delta\text{H}_2\text{O}(P) \cdot (10^{-6}) \cdot \frac{18.02 \frac{\text{g}}{\text{mole}} \text{ H}_2\text{O}}{28.97 \frac{\text{g}}{\text{mole}} \text{ AIR}} \cdot 10^2 \text{ dP in [kt]}.$$

Area(*P*) is either a constant area of 20,000 km<sup>2</sup> or allowed to vary with pressure, *P*, in hPa;  $\Delta\text{H}_2\text{O}(P)$  is the absolute difference in water vapor mixing ratio in ppmv as a function of pressure; and  $g = 9.81 \text{ m/s}^2$ . For a constant minimum area estimate of 20,000 km<sup>2</sup> throughout the column, the calculation yields a total change in water vapor mass of +6.9 kt (with 1 tonne (t) = 1000 kg) when the measurements on descent are used and +6.3 kt when the measurements on ascent are used. When we allow for a rapid decrease in area with altitude from a maximum at the tropopause (115 hPa) of 100,000 km<sup>2</sup>, we obtain an added water vapor mass estimate of  $13.5 \pm 1.7$  kt. We conclude, therefore, that the MN-WI storm system identified above irreversibly delivered approximately 6.6–13.5 kt of water to the stratosphere, based upon the in situ observations acquired 10–20 h downstream from the storm.

**Table 1.** Estimated Percentage Increase in Stratospheric Water Vapor Over a Column Extending From 115 hPa to 70 hPa Due to the Case Study Storm System for Different Geographical Regions<sup>a</sup>

H <sub>2</sub> O Added 6.6 kt (13.5 kt)	Area (km <sup>2</sup> )	Mass Air (kt)	Mass H <sub>2</sub> O (kt) Background = 5 ppmv	% H <sub>2</sub> O Mass Added
Plume (41.5°–42.6°N; 91°–89°W)	$2.02 \times 10^4$ ( $1.00 \times 10^5$ )	$9.27 \times 10^6$	$2.88 \times 10^1$	23
CONUS mid/NAMA (25°–50°N; 80°–105°W)	$6.08 \times 10^6$	$2.79 \times 10^9$	$8.68 \times 10^3$	0.08 (0.16)
CONUS 30–50 (30°–50°N; 65°–125°W)	$1.13 \times 10^7$	$5.19 \times 10^9$	$1.61 \times 10^4$	0.04 (0.08)
Zonal (30°–50°N; 180°W–180°E)	$6.79 \times 10^7$	$3.11 \times 10^{10}$	$9.68 \times 10^4$	0.007 (0.014)

<sup>a</sup>The first column defines the bounds for each geographic region, the second displays the area of the region in km<sup>2</sup>, the third provides an estimate of the mass of air contained with the volume described by the area and the 115 hPa to 70 hPa pressure levels, the fourth provides an estimate of the mass of water in the given volume assuming a constant background mixing ratio of 5 ppmv, and the fifth shows the percentage increase in water vapor resulting from an addition of 6.6 kt (13.2 kt) of water, the amount attributed to the case study storm system as determined from observations 10–20 h downstream.

To determine the contribution of this storm system to larger geographical regions we must make an assumption about the representative unperturbed (or background) mass of water in the stratosphere. The simplest approach is to assume a constant stratospheric water vapor profile of 5 ppmv. The corresponding mass in the column between 115 hPa and 70 hPa can then be computed for different geographical regions, with

$$[\text{Mass AIR in Column}]_{115-70 \text{ hPa}} = \text{Area} \cdot (1/g) \cdot (P_{115} - P_{70}) \cdot 10^2 \text{ in [kt]}, \text{ and}$$

$$[\text{Mass Background H}_2\text{O in Column}]_{115-70 \text{ hPa}} = \frac{[\text{Mass AIR in Column}] \cdot 5 \times 10^{-6} \cdot (18.02 \frac{\text{g}}{\text{mole}} \text{ H}_2\text{O})}{28.97 \frac{\text{g}}{\text{mole}} \text{ AIR}} \text{ in [kt]}$$

for a constant water vapor mixing ratio of 5 ppmv and Area in km<sup>2</sup>. In these calculations, we use a constant area through the column. Table 1 shows the results of this approach. Using this method, the estimated percentage increase in water vapor due to an integrated addition of 6.6 kt over a column extending from 115 hPa to 70 hPa with an area of 20,000 km<sup>2</sup> is 23%. Note that this result, which utilizes an assumed constant background mixing ratio of 5 ppmv, is consistent with the more precise calculations shown in Figure 12. The percentage contribution of this plume to larger geographical regions drops off as the fractional area occupied by the plume decreases. For example, the estimated percentage increase for a region encompassing the NAMA, i.e., 25°N–50°N and 80°W–105°W, is ~0.08% (~0.16%), and for a zonal band over CONUS, i.e., 30°N–50°N and 65°W–125°W, it is ~0.04% (~0.08%). The values in parentheses represent estimates for the larger mass estimate. Globally, the total water vapor content of the stratosphere at pressures <100 hPa is ~1000 Tg or  $1 \times 10^6$  kt. Thus, in the context of the stratospheric water vapor budget, the contribution of this case-study storm system ranges from ~0.0007 to 0.0013%.

In order to place the individual storm system analyzed here within both a regional and global context, we next examine aircraft and satellite climatologies of extreme events.

#### 4.2. In Situ Climatology of Water Vapor Extrema Over North America in Summer

In situ water vapor data acquired by HWV (10 s) over 10 airborne missions from 1995 to 2013 are plotted as a function of potential temperature and color-coded by season in Figure 13. The panels correspond to three distinct geographical regions over North America. The greatest frequency of observed water vapor extrema is in the late spring and summer months (May–June and July–August) over the central U.S.

These figures reveal three primary seasonal and geographical features of UTLS water vapor over North America. (1) a seasonal cycle in water vapor is evident throughout the UTLS at levels below 440 K, with mean values in the lower stratosphere higher in the late summer and early fall and lower in the winter and spring. This result is broadly consistent with the analysis of 30 years of water vapor data acquired on soundings launched from Boulder, CO [Hurst et al., 2011]. As Hurst et al. [2011] noted, both the magnitude and phase of the seasonal cycle in water vapor evident at midlatitudes are consistent with the rapid transport of this signal from the tropical lower stratosphere [e.g., Mote et al., 1996] to higher latitudes. (2) A difference in the frequency and magnitude of water vapor extrema is evident for the spring/summer data acquired west of the Rocky Mountains and the data acquired over the central and eastern U.S. Of the three regions plotted, the greatest number of extrema is observed over the central and eastern U.S. throughout late spring and summer. (3) There is a notable difference in the frequency of these extrema between the data acquired at midlatitudes (30°–50°N) and data acquired in the subtropics south of 30°N, with the greater frequency of high water vapor observations at midlatitudes. For this multimission data set the number of observations obtained

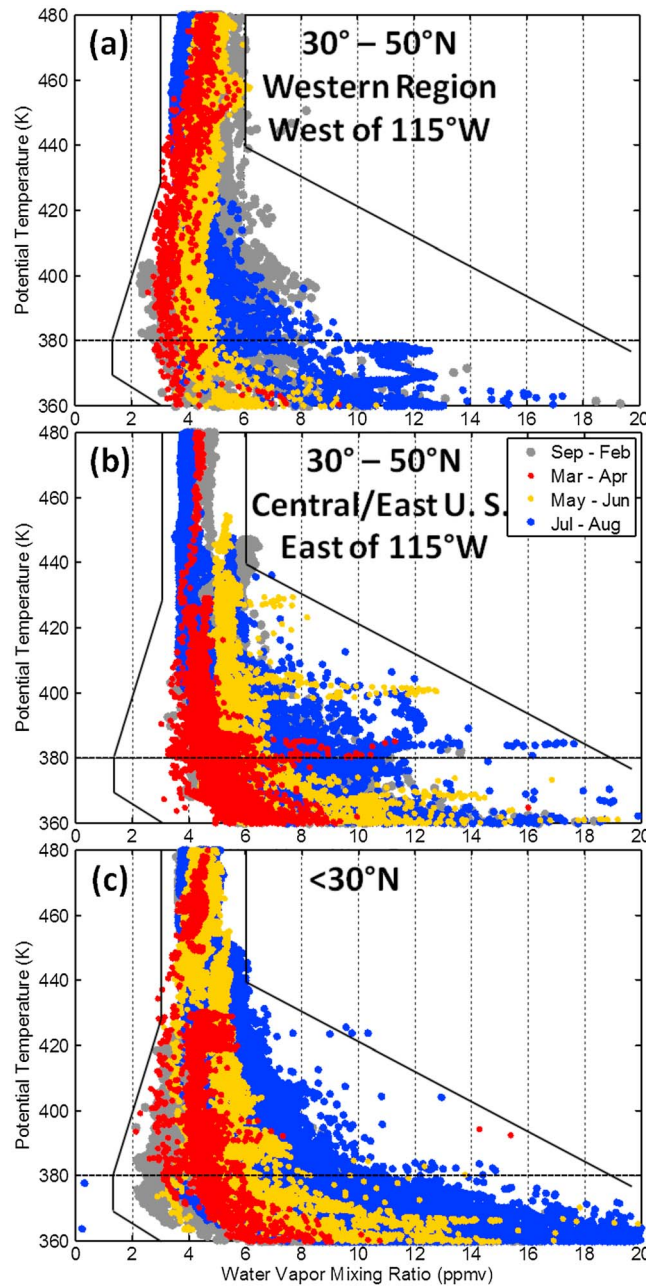


**Figure 13.** Vertical profiles of in situ water vapor data over the U.S. showing when and where water vapor extrema have been observed. Water vapor data from multiple missions measured in situ by HWV (10 s) are plotted as a function of potential temperature (K). The colors correspond to period, with the convectively quiescent period between September and February in gray, and the periods of most frequent overshooting convection occurring in the late spring and summer months in yellow and blue. The thin black lines defining the nominal envelope of the observations are the same in each plot. (a) Water vapor data selected to be between 135° and 115°W and between 30° and 50°N. (b) Water vapor data selected to be between 115° and 65°W and between 30° and 50°N. (c) Water vapor data selected to be between 135°W and 65°W and located south of 30°N.

at latitudes  $<30^{\circ}\text{N}$  is 30% higher than the number obtained over the central U.S. during July and August in the potential temperature range of interest. Thus, while aircraft missions are inherently limited in both their temporal and spatial sampling capabilities, sampling cannot explain why the central U.S. in summer exhibits a greater frequency of extrema.

While aircraft missions are inherently limited in both their temporal and spatial sampling capabilities, the fact that the central U.S. in summer exhibits a greater frequency of extrema is unlikely a result of sampling. For this multimission data set the number of observations obtained over the central U.S. during July and August in the potential temperature range of interest, 360 to 480 K, is 30% lower than the number obtained at latitudes  $<30^{\circ}\text{N}$ .

The correspondence between the regional and seasonal distribution of deep, tropopause-penetrating convective storms and the frequency distribution of water vapor enhancements in the observational data set, including in the case study analysis presented here, suggests that these storms are the most likely cause of the observed extrema. Furthermore, in situ and satellite observations of enrichments in the heavy isotopologue of water, HDO, on both the plume scale [Hanisco et al., 2007] and the regional scale [Sayres et al., 2010; Randel et al., 2012; Sargent et al., 2014], provide additional confirmation that the extrema result from the irreversible delivery of water vapor as ice lofted by convection into the stratosphere over the U.S. in summer.

### 4.3. MLS Satellite Climatology of Water Vapor Extrema Over North America in Summer

The Earth Observing System Microwave Limb Sounder (MLS) aboard the NASA Aura satellite

provides a homogeneous, near-global ( $82^{\circ}\text{N}$  to  $82^{\circ}\text{S}$ ) observational data set of many important trace species, including water vapor in the UTLS [Read et al., 2007; Livesey et al., 2011, 2016]. Since its launch in

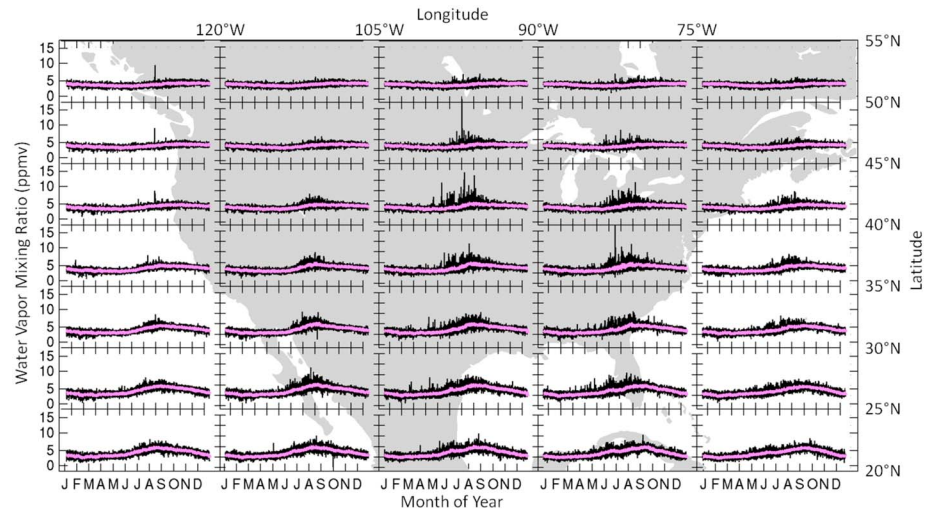


**Figure 14.** Time series of geographically binned MLS water vapor at 100 hPa. Daily time series of 100 hPa water vapor retrievals for each year from 2005 to 2016 are plotted (black traces) in boxes superimposed over their corresponding geographical region. The daily mean values over the 12 year period for each geographical bin are shown in pink. These data reveal the seasonal and regional localization of the water vapor extrema.

July 2004, MLS has supplied near continuous measurements leading to a long and valuable data set for investigating the stratospheric water vapor budget, as well as seasonal-to-decadal scale variability in UTLS water vapor. The stated uncertainty of the MLS water vapor product is ~10% at 100 hPa [Read et al., 2007], and the spatial resolution is 3 km in the vertical and approximately 200 km in the horizontal. In the following analysis, we use version 4.2 water vapor data at 100 hPa and follow the quality-control recommendations of the MLS science team [Livesey et al., 2011, 2016]. There are some important limitations to the MLS observations: (1) the sparse sampling of the North American continent on any individual day and (2) the vertical and horizontal averaging, which significantly impacts both the number of extreme events observed and their absolute magnitude. Despite these considerations, the broader statistics evident in the geographical and seasonal distributions of MLS data shown below are robust and informative.

An examination of MLS monthly or seasonally averaged water vapor at 100 hPa reveals significant summertime enhancements over two regions in the Northern Hemisphere, the Himalayas in the Asian sector and the central to southeastern U.S. in North America [Ploeger et al., 2013; Randel et al., 2015; Dessler and Sherwood, 2004]. Both regions occur in conjunction with upper-level anticyclonic circulations in proximity to monsoons [Dunkerton, 1995; Gettelman et al., 2004]. This signal is also evident in analyses of other satellite data sets, such as the Halogen Occultation Experiment and Atmospheric Composition Experiment-Fourier Transform Spectrometer satellite instruments [Randel et al., 2001, 2012]. Additionally, applying a threshold of >8 ppmv at 100 hPa, Schwartz et al. [2013] report a high frequency of water vapor extrema in the same two regions in summer. In Figure 2 of Schwartz et al. [2013], the region with the greatest frequency of water vapor extrema over Asia is centered near 25°–30°N and not clearly isolated from the subtropics. In contrast, the observations of high water vapor over the U.S. extend to 50°N, where subtropical influence is significantly less likely and local tropopause-penetrating convection is more probable.

Aggregate results of individual water vapor retrievals by MLS reveal many of the same features as the aircraft climatology. In Figure 14 we show superimposed time series (black traces) of all MLS retrievals of water vapor at 100 hPa for each year within a 12 year period (2005–2016) subdivided by geographical region (35 geographic bins encompassing CONUS). The data shown in each bin were acquired within the bounds of the underlying latitude-longitude area, and the corresponding regional daily mean value for the 12 year record is overlaid in pink. This figure shows the seasonal cycle in the underlying mean, as well as the variation in the amplitude of the mean as a function of geographic location. The seasonal and geographical dependence of the water vapor extrema is also evident.

Similar to what was found in the analysis of the in situ data, and consistent with the analysis of Schwartz et al. [2013], Figure 14 reveals several features about water vapor in the lower stratosphere over North America.

(1) The seasonal cycle in the mean is evident at 100 hPa with the summertime maximum prominent at subtropical latitudes and also evident at higher latitudes. (2) Many extreme water vapor mixing ratios are observed by MLS. Because of vertical and horizontal averaging, the absolute magnitude of these observations is less than, but qualitatively similar to, the enhancements observed in situ by HWV. (3) As in the aircraft climatology, these extrema appear almost exclusively within the continental interior, primarily over the Great Plains east of the Rocky Mountains, and are observed as far north as 50°N. (4) There is a strong seasonality in the occurrence of these anomalous water vapor enhancements. The extrema are observed preferentially in the months of June, July, and August, with peak frequency in July and August. (5) The total number of water vapor extrema in the summertime over CONUS (30°–50°N; 65°–125°W) exhibits large interannual variability, with some years registering as many as 4 times the mean number. In summary, the seasonal and geographic distribution of water vapor extrema evident in the MLS data set supports the conclusions drawn from the more limited, but higher resolution, aircraft data set.

It is clear from both the in situ and satellite climatologies that the occurrence of stratospheric water vapor extrema is highly dependent upon both geographic region and season. In the western hemisphere, the central and southeastern U.S. in summer reveals not only the greatest frequency of these extrema but also the largest magnitude water vapor mixing ratios. The case study plume encountered on the 27 August 2013 flight is an example of one such extremum, and we have tied the high water vapor mixing ratios evident in this plume to a convective storm system that occurred approximately 12 h prior to the aircraft encounter. Given the high frequency of tropopause-penetrating storms over this region and season evident in NEXRAD data, it is likely that local convection is a dominant source of these extrema.

## 5. Conclusions

Deep convection over the central and eastern U.S. frequently penetrates the tropopause level. Turbulent processes associated with overshooting convective cores can lead to the detrainment and mixing of water, predominantly as ice, which rapidly sublimates in the subsaturated environment. This mechanism provides a means of irreversibly delivering water vapor directly into both the middleworld and overworld stratosphere, bypassing the thermal control of tropical cold-point tropopause temperatures, which is considered to be the primary constraint on stratospheric humidity. Moist plumes arising from these events are evident as water vapor extrema in both high-resolution aircraft and global satellite data.

The SEAC<sup>4</sup>RS field mission staged out of Houston, TX, during the summer of 2013 provided multiple opportunities to sample convective outflow in the stratosphere with the high-resolution capabilities of NASA's ER-2 high-altitude research aircraft. On the flight of 27 August 2013, the aircraft encountered a region of enhanced water vapor, extending over a depth of ~2 km in the overworld (~380 K to 415 K), south of the Great Lakes. The plume was sampled during the fourth vertical dive of the flight. The locations of the aircraft encounter on descent at its western edge (42.58°N, 90.96°W, 27 August 2013 19:40 UTC) and ascent at its eastern edge (41.54°, 89.00°W, 27 August 2013 20:00 UTC) are used to infer a minimum plume area of 20,000 km<sup>2</sup>. Water vapor mixing ratios in the plume, measured in situ by HWV, reached 12 ppmv (8 ppmv above the nominal background) in an upper lobe between 400 K and 415 K potential temperature and reached 18 ppmv (11 ppmv above the nominal background) in a lower lobe between 375 K and 385 K potential temperature. The magnitude of water vapor in this plume was unprecedented for the high potential temperatures and latitudes at which it was observed.

Complementary data products derived from satellite and ground-based sources, in conjunction with isentropic trajectory calculations, allow for the identification and characterization of the contributing storm system. An OT detection product, derived from GOES-13 IR imagery, offers a comprehensive record of convective activity over CONUS for the period of the SEAC<sup>4</sup>RS mission, and back trajectories provide the means to tie individual points within the plume encounter to individual OTs. Results of the OT and BT analysis show that a storm system that developed and matured over Minnesota and Wisconsin between 26 August 2013 21:00 UTC and 27 August 2013 12:00 UTC was the most likely convective source for the elevated water vapor observed in situ on 27 August 2013.

A high-resolution 3-D data product derived from the NEXRAD network gives a detailed picture of the structure and history of this storm. The data demonstrate both the instantaneous penetration of the tropopause, up to ~4 km into the stratosphere and 450 K potential temperature, in the convective core of one storm cell,

as well as the long (>2 h) history of several independent storms within the larger system. The radar data confirm that a considerable area of the lower stratosphere was exposed to convective influence, leading to the large enhancement in water vapor observed in situ approximately 10 to 20 h downstream. Similarly, super rapid scan GOES satellite imagery in both the visible and infrared provide an independent method of visualizing the evolution of OTs and detrained plumes above the anvil.

Vertical sampling by the ER-2 makes it possible to calculate the net fractional change in the water vapor column and to estimate the integrated quantity of water irreversibly transported to the overworld by this particular storm system. Analysis of the in situ data shows that column water vapor over a range from 115 hPa to 70 hPa was elevated by ~22%, and estimates of the total mass of water vapor added to the lower stratosphere are found to be between +6.6 kt and +13.5 kt approximately 10–20 h after convection. While the contribution of this storm system is found to be small, ~0.08%–0.16% in the NAMA region, the integrated effect of multiple storms over a period of a week or two, resulting from the confinement of air parcels within the NAMA circulation, may become significant, particularly during years of frequent convection.

Both in situ and satellite climatologies of water vapor extrema show that the frequency of these events in the Western Hemisphere is largest over the central and south-central U.S. in summer, broadly consistent with the geographical and seasonal distribution of tropopause-penetrating convective storms. More work is needed to quantitatively link the observations of overshooting convection in the GOES and NEXRAD composites with the observations of both stratospheric water vapor extrema and the enhancement in mean water vapor over the U.S. in summer. Similarly, analysis of the impact of convection on the broader chemical composition of this region and season is warranted. Given the potential sensitivity of convective frequency and/or strength to increased climate forcing from rising greenhouse gas concentrations, it is important that the details of this mechanism be understood.

#### Acknowledgments

We thank the pilots and crew of the NASA ER-2, the logistical support provided by NASA, and the engineering staff of the Harvard group, for making the HWV measurements possible. Participation of HWV in the SEAC<sup>4</sup>RS mission was supported by NASA grant NNX12AN06G, and subsequent data analysis was supported by NASA grant NNX15AC29G under NASA's Atmospheric Composition focus area. K.M.B. acknowledges funding for the development of the OT product by the NOAA GOES-R Risk Reduction Research Program. K.P.B. and C.R.H. received support from the National Science Foundation through grants 1522906 and 1522910, and D.M.W. received support from NASA grant NNX15AD87G. SEAC<sup>4</sup>RS mission ER-2 aircraft data and GOES analysis products are available from the NASA Langley Research Center (LaRC) Airborne Science Data for Atmospheric Composition archive (<https://www-air.larc.nasa.gov/mis-sions/seac4rs/index.html>). Data from the interim reanalysis from the European Centre for Medium-Range Weather Forecasts (ERA-I) used for the back trajectories can be downloaded from the Research Data Archive at the National Center for Atmospheric Research (<http://rda.ucar.edu/datasets/ds627.0/>). The original NEXRAD data are available through the NOAA National Centers for Environmental Information (NCEI) site (<https://www.ncdc.noaa.gov/data-access/radar-data/nexrad/>). The files were translated to netCDF format using the NOAA Weather and Climate Toolkit (<https://www.ncdc.noaa.gov/wct/>). MLS can be downloaded from the Goddard Earth Sciences Data and Information Services Center archive (<https://mirador.gsfc.nasa.gov/>). We would also like to thank Jan Kanak (Slovak Hydrometeorological Institute) for deriving the GOES-14 visible shadow-based OT penetration depths and Jack W. Cooney for sharing the results of his ongoing processing and analysis of the 10 year NEXRAD climatology.

#### References

- Anderson, J. G., D. M. Wilmoth, J. B. Smith, and D. S. Sayres (2012), UV dosage levels in summer: Increased risk of ozone loss from convectively injected water vapor, *Science*, 337(6096), 835–839.
- Anderson, J. G., et al. (2017), Stratospheric ozone over the United States in summer linked to observations of convection and temperature via chlorine and bromine catalysis, *PNAS*, 114(25), E4905–E4913.
- Andrews, D. G., et al. (1987), *Middle Atmosphere Dynamics*, p. 3, Academic Press, San Diego, Calif.
- Bedka, K. M. (2011), Overshooting cloud top detections using MSG SEVIRI infrared brightness temperatures and their relationship to severe weather over Europe, *Atmos. Res.*, 99(2), 175–189.
- Bedka, K. M., J. Brunner, R. Dworak, W. Feltz, J. Otkin, and T. Greenwald (2010), Objective satellite-based overshooting top detection using infrared window channel brightness temperature gradients, *J. Appl. Meteorol. Climatol.*, 49(2), 181–202.
- Bedka, K. M., R. Dworak, J. Brunner, and W. Feltz (2012), Validation of satellite-based objective overshooting cloud-top detection methods using CloudSat cloud profiling radar observations, *J. Appl. Meteorol. Climatol.*, 51(10), 1811–1822.
- Bedka, K. M., C. Wang, R. Rogers, L. Carey, W. Feltz, and J. Kanak (2015), Examining deep convective cloud evolution using total lightning, WSR-88D, and GOES-14 super rapid scan datasets, *Weather Forecasting*, 30, 571–590.
- Booth, J. F., S. Wang, and L. M. Polvani (2012), Midlatitude storms in a moister world: Lessons from idealized baroclinic life cycle experiments, *Clim. Dyn.*, 41(3–4), 787–802.
- Bowman, K. P. (1993), Large-scale isentropic mixing properties of the Antarctic polar vortex from analyzed winds, *J. Geophys. Res.*, 98, 23,013–23,027.
- Bowman, K. P., and G. R. Carre (2002), The mean-meridional transport circulation of the troposphere in an idealized GCM, *J. Atmos. Sci.*, 59, 1502–1514.
- Bowman, K. P., L. L. Pan, T. Campos, and R. Gao (2007), Observations of fine-scale transport structure in the upper troposphere from the high-performance instrumented airborne platform for environmental research, *J. Geophys. Res.*, 112, D18111, doi:10.1029/2007JD008685.
- Bowman, K. P., J. C. Lin, A. Stohl, R. Draxler, P. Konopka, A. Andrews, and D. Brunner (2013), Input data requirements for Lagrangian trajectory models, *Bull. Am. Meteorol. Soc.*, 94, 1051–1058.
- Brewer, A. W. (1949), Evidence for a world circulation provided by the measurements of helium and water vapour distribution in the stratosphere, *Q. J. R. Meteorol. Soc.*, 75(326), 351–363.
- Brooks, H. E., J. W. Lee, and J. P. Craven (2003), The spatial distribution of severe thunderstorm and tornado environments from global reanalysis data, *Atmos. Res.*, 67, 73–94.
- Carslaw, K. S., B. P. Luo, and T. Peter (1995), An analytic-expression for the composition of aqueous HNO<sub>3</sub>-H<sub>2</sub>SO<sub>4</sub> stratospheric aerosols including gas-phase removal of HNO<sub>3</sub>, *Geophys. Res. Lett.*, 22(14), 1877–1880.
- Carslaw, K. S., T. Peter, and S. L. Clegg (1997), Modeling the composition of liquid stratospheric aerosols, *Rev. Geophys.*, 35(2), 125–154.
- Corti, T., et al. (2008), Unprecedented evidence for deep convection hydrating the tropical stratosphere, *Geophys. Res. Lett.*, 35, L10810, doi:10.1029/2008GL033641.
- Crum, T. D., and R. L. Albery (1993), The WSR-88D and the WSR-88D operational support facility, *Bull. Am. Meteorol. Soc.*, 74(9), 1669–1687.
- Dee, D. P., et al. (2011), The ERA-interim reanalysis: Configuration and performance of the data assimilation system, *Q. J. R. Meteorol. Soc.*, 137, 553–597.
- de Reus, M., et al. (2009), Evidence for ice particles in the tropical stratosphere from in-situ measurements, *Atmos. Chem. Phys.*, 9, 6775–6792.
- Dessler, A. E., and S. C. Sherwood (2004), Effect of convection on the summertime extratropical lower stratosphere, *J. Geophys. Res.*, 109, D23301, doi:10.1029/2004JD005209.

- Dessler, A. E., E. J. Hints, E. M. Weinstock, J. G. Anderson, and K. R. Chan (1995), Mechanisms controlling water vapor in the lower stratosphere: "A tale of two stratospheres", *J. Geophys. Res.*, *100*(D11), 23,167–23,172.
- Dessler, A. E., T. F. Hanisco, and S. Fueglistaler (2007), Effects of convective ice lofting on H<sub>2</sub>O and HDO in the tropical tropopause layer, *J. Geophys. Res.*, *112*, D18309, doi:10.1029/2007JD008609.
- Dessler, A. E., M. R. Schoeberl, T. Wang, S. M. Davis, and K. H. Rosenlof (2013), Stratospheric water vapor feedback, *Proc. Natl. Acad. Sci. U.S.A.*, *110*, 18,087–18,091.
- Doswell, C. A., III, and L. F. Bosart (2001), Extratropical synoptic-scale processes and severe convection, in *Severe Convective Storms*, pp. 27–69, American Meteorological Society, Boston, Mass.
- Dunkerton, T. J. (1995), Evidence of meridional motion in the summer lower stratosphere adjacent to monsoon regions, *J. Geophys. Res.*, *100*(D8), 16,675–16,688.
- Drdla, K., and R. Müller (2012), Temperature thresholds for chlorine activation and ozone loss in the polar stratosphere, *Ann. Geophys.*, *30*(7), 1055–1073.
- Fischer, H., et al. (2003), Deep convective injection of boundary layer air into the lowermost stratosphere at midlatitudes, *Atmos. Chem. Phys.*, *3*(3), 739–745.
- Forster, P. M. D., and K. P. Shine (1999), Stratospheric water vapour changes as a possible contributor to observed stratospheric cooling, *Geophys. Res. Lett.*, *26*(21), 3309–3312.
- Forster, P. M. D., and K. P. Shine (2002), Assessing the climate impact of trends in stratospheric water vapor, *Geophys. Res. Lett.*, *29*(6), 10-1–10-4, doi:10.1029/2001GL013909.
- Fueglistaler, S., M. Bonazzola, P. H. Haynes, and T. Peter (2005), Stratospheric water vapor predicted from the Lagrangian temperature history of air entering the stratosphere in the tropics, *J. Geophys. Res.*, *110*, D08107, doi:10.1029/2004JD005516.
- Fueglistaler, S., A. E. Dessler, T. J. Dunkerton, I. Folkins, Q. Fu, and P. W. Mote (2009), Tropical tropopause layer, *Rev. Geophys.*, *47*, RG1004, doi:10.1029/2008RG000267.
- Fueglistaler, S., Y. S. Liu, T. J. Flannaghan, F. Ploeger, and P. H. Haynes (2014), Departure from Clausius-Clapeyron scaling of water entering the stratosphere in response to changes in tropical upwelling, *J. Geophys. Res. Atmos.*, *119*, 1962–1972, doi:10.1002/2013JD020772.
- Gaines, S. E., S. W. Bowen, R. S. Hipskind, T. P. Bui, and K. R. Chan (1992), Comparisons of the NASA ER-2 meteorological measurement system with radar tracking and radiosonde data, *J. Atmos. Oceanic Technol.*, *9*, 210–225.
- Gettelman, A., D. E. Kinnison, T. J. Dunkerton, and G. P. Brasseur (2004), Impact of monsoon circulations on the upper troposphere and lower stratosphere, *J. Geophys. Res.*, *109*, D22101, doi:10.1029/2004JD004878.
- Gill, A. E. (1980), Some simple solutions for heat-induced tropical circulation, *Q. J. R. Meteorol. Soc.*, *106*, 447–462.
- Griffin, S., K. M. Bedka, and C. S. Velden (2016), A method for calculating the height of overshooting convective cloud tops using satellite-based IR imager and CloudSat cloud profiling radar observations, *J. Appl. Meteorol. Climatol.*, *55*, 479–491.
- Grosvenor, D. P., T. W. Choulaton, H. Coe, and G. Held (2007), A study of the effect of overshooting deep convection on the water content of the TTL and lower stratosphere from cloud resolving model simulations, *Atmos. Chem. Phys.*, *7*, 4977–5002.
- Hanisco, T. F., et al. (2001), Sources, sinks, and the distribution of OH in the lower stratosphere, *J. Phys. Chem. A*, *105*(9), 1543–1553.
- Hanisco, T. F., et al. (2002), Quantifying the rate of heterogeneous processing in the Arctic polar vortex with in situ observations of OH, *J. Geophys. Res.*, *107*(D20), 8278, doi:10.1029/2001JD000425.
- Hanisco, T. F., et al. (2007), Observations of deep convective influence on stratospheric water vapor and its isotopic composition, *Geophys. Res. Lett.*, *34*, L04814, doi:10.1029/2006GL027899.
- Hegglin, M. I., et al. (2004), Tracing troposphere-to-stratosphere transport above a mid-latitude deep convective system, *Atmos. Chem. Phys.*, *4*(3), 741–756.
- Held, I. M., and B. J. Soden (2000), Water vapor feedback and global warming, *Annu. Rev. Energy Environ.*, *25*, 441–475.
- Hints, E. J., E. M. Weinstock, J. G. Anderson, R. D. May, and D. F. Hurst (1999), On the accuracy of in situ water vapor measurements in the troposphere and lower stratosphere with the Harvard Lyman- $\alpha$  hygrometer, *J. Geophys. Res.*, *104*(D7), 8183–8189.
- Holton, J. R. (2004), *An Introduction to Dynamic Meteorology*, Academic, New York.
- Holton, J. R., and A. Gettelman (2001), Horizontal transport and the dehydration of the stratosphere, *Geophys. Res. Lett.*, *28*(14), 2799–2802.
- Holton, J. R., P. H. Haynes, M. E. McIntyre, A. R. Douglass, R. B. Rood, and L. Pfister (1995), Stratosphere-troposphere exchange, *Rev. Geophys.*, *33*(4), 403–439.
- Homeyer, C. R. (2014), Formation of the enhanced-V infrared cloud-top feature from high-resolution three-dimensional radar observations, *J. Atmos. Sci.*, *71*(1), 332–348.
- Homeyer, C. R., and M. R. Kumjian (2015), Microphysical characteristics of overshooting convection from polarimetric radar observations, *J. Atmos. Sci.*, *72*(2), 870–891.
- Homeyer, C. R., L. L. Pan, and M. C. Barth (2014a), Transport from convective overshooting of the extratropical tropopause and the role of large-scale lower stratosphere stability, *J. Geophys. Res. Atmos.*, *119*, 2220–2240, doi:10.1002/2013JD020931.
- Homeyer, C. R., et al. (2014b), Convective transport of water vapor into the lower stratosphere observed during double-tropopause events, *J. Geophys. Res. Atmos.*, *119*, 10,941–10,958, doi:10.1002/2014JD021485.
- Homeyer, C. R., J. D. McAuliffe, and K. M. Bedka (2017), On the development of above-anvil cirrus plumes in extratropical convection, *J. Atmos. Sci.*, *74*, 1617–1633.
- Hoskins, B. J. (1991), Towards a PV- $\theta$  view of the general circulation, *Tellus B*, *43*, 27–35.
- Hurst, D. F., S. J. Oltmans, H. Vömel, K. H. Rosenlof, S. M. Davis, E. A. Ray, E. G. Hall, and A. F. Jordan (2011), Stratospheric water vapor trends over Boulder, Colorado: Analysis of the 30 year Boulder record, *J. Geophys. Res.*, *116*, D02306, doi:10.1029/2010JD015065.
- Iwasaki, S., T. Shibata, J. Nakamoto, H. Okamoto, H. Ishimoto, and H. Kubota (2010), Characteristics of deep convection measured by using the A-train constellation, *J. Geophys. Res.*, *115*, D06207, doi:10.1029/2009JD013000.
- Jensen, E., and L. Pfister (2004), Transport and freeze-drying in the tropical tropopause layer, *J. Geophys. Res.*, *109*, D02207, doi:10.1029/2003JD004022.
- Jensen, E. J., et al. (2005), Ice supersaturations exceeding 100% at the cold tropical tropopause: Implications for cirrus formation and dehydration, *Atmos. Chem. Phys.*, *5*, 851–862.
- Jensen, E., A. S. Ackerman, and J. A. Smith (2007), Can overshooting convection dehydrate the tropical tropopause layer?, *J. Geophys. Res.*, *112*, D11209, doi:10.1029/2006JD007943.
- Jensen, E. J., G. Diskin, R. P. Lawson, S. Lance, T. P. Bui, D. Hlavka, M. McGill, L. Pfister, O. B. Toon, and R. Gao (2013), Ice nucleation and dehydration in the tropical tropopause layer, *Proc. Natl. Acad. Sci. U.S.A.*, *110*(6), 2041–2046.
- Jost, H.-J., et al. (2004), In-situ observations of mid-latitude forest fire plumes deep in the stratosphere, *Geophys. Res. Lett.*, *31*, L11101, doi:10.1029/2003GL019253.

- Khaykin, S., J.-P. Pommereau, L. Korshunov, V. Yushkov, J. Nielsen, N. Larsen, T. Christensen, A. Garnier, A. Lukyanov, and E. Williams (2009), Hydration of the lower stratosphere by ice crystal geysers over land convective systems, *Atmos. Chem. Phys.*, *9*, 2275–2287.
- Khaykin, S. M., J.-P. Pommereau, E. D. Riviere, G. Held, F. Ploeger, M. Ghysels, N. Amarouche, J.-P. Vernier, F. G. Wienhold, and D. Ionov (2016), Evidence of horizontal and vertical transport of water in the Southern Hemisphere tropical tropopause layer (TTL) from high-resolution balloon observations, *Atmos. Chem. Phys.*, *16*, 12,273–12,286.
- Kley, D., A. L. Schmeltekopf, K. Kelly, R. H. Winkler, T. L. Thompson, and M. McFarland (1982), Transport of water through the tropical tropopause, *Geophys. Res. Lett.*, *9*, 617–620.
- Koby, T. (2016), Development of a trajectory model for the analysis of stratospheric water vapor, Doctoral dissertation, School of Engineering and Applied Sciences, Harvard Univ.
- Laing, A. G., and J. M. Fritsch (1997), The global population of mesoscale convective complexes, *Q. J. R. Meteorol. Soc.*, *123*(538), 389–405.
- Le, T. V., and W. A. Gallus Jr. (2012), Effect of an extratropical mesoscale convective system on water vapor transport in the upper troposphere/lower stratosphere: A modeling study, *J. Geophys. Res.*, *117*, D03111, doi:10.1029/2011JD016685.
- Liang, Q., E. Atlas, D. Blake, M. Dorf, K. Pfeilsticker, and S. Schauffler (2014), Convective transport of very short lived bromocarbons to the stratosphere, *Atmos. Chem. Phys.*, *14*, 5781–5792.
- Livesey, N. J., et al. (2011), Version 3.3 level 2 data quality and description document, JPL D-33509.
- Livesey, N. J., et al. (2016), Version 4.2x level 2 data quality and description document, JPL D-33509 Rev. B.
- Liu, N., and C. Liu (2016), Global distribution of deep convection reaching tropopause in 1 year GPM observations, *J. Geophys. Res. Atmos.*, *121*, 3824–3842, doi:10.1002/2015JD024430.
- Minnis, P., C. R. Yost, S. Sun-Mack, and Y. Chen (2008), Estimating the top altitude of optically thick ice clouds from thermal infrared satellite observations using CALIPSO data, *Geophys. Res. Lett.*, *35*, L12801, doi:10.1029/2008GL033947.
- Mote, P. W., K. H. Rosenlof, M. E. McIntyre, E. S. Carr, J. C. Gille, J. R. Holton, J. S. Kinnersley, H. C. Pumphrey, J. M. Russell, and J. W. Waters (1996), An atmospheric tape recorder: The imprint of tropical tropopause temperatures on stratospheric water vapor, *J. Geophys. Res.*, *101*(D2), 3989–4006.
- Mullendore, G. L., D. R. Durran, and J. R. Holton (2005), Cross-tropopause tracer transport in midlatitude convection, *J. Geophys. Res.*, *110*, D06113, doi:10.1029/2004JD005059.
- Pittman, J. V., et al. (2007), Transport in the subtropical lowermost stratosphere during the Cirrus Regional Study of Tropical Anvils and Cirrus Layers—Florida Area Cirrus Experiment, *J. Geophys. Res.*, *112*, D08304, doi:10.1029/2006JD007851.
- Ploeger, F., G. Gunther, P. Konopka, S. Fueglistaler, R. Muller, C. Hoppe, A. Kunz, R. Spang, J. U. Grooss, and M. Riese (2013), Horizontal water vapor transport in the lower stratosphere from subtropics to high latitudes during boreal summer, *J. Geophys. Res. Atmos.*, *118*, 8111–8127, doi:10.1002/jgrd.50636.
- Poulida, O., R. R. Dickerson, and A. Heymsfield (1996), Stratosphere-troposphere exchange in a midlatitude mesoscale convective complex: 1. Observations, *J. Geophys. Res.*, *101*(D3), 6823–6836.
- Randel, W. J., K. Zhang, and R. Fu (2015), What controls stratospheric water vapor in the NH summer monsoon regions? *J. Geophys. Res. Atmos.*, *120*, 7988–8001, doi:10.1002/2015JD023622.
- Randel, W. J., E. Moyer, M. Park, E. Jensen, P. Bernath, K. Walker, and C. Boone (2012), Global variations of HDO and HDO/H<sub>2</sub>O ratios in the upper troposphere and lower stratosphere derived from ACE-FTS satellite measurements, *J. Geophys. Res.*, *117*, D06303, doi:10.1029/2011JD016632.
- Randel, W. J., F. Wu, A. Gettelman, J. M. Russell, J. M. Zawodny, and S. J. Oltmans (2001), Seasonal variation of water vapor in the lower stratosphere observed in Halogen Occultation Experiment data, *J. Geophys. Res.*, *106*(D13), 14,313–14,325.
- Ray, E. A., et al. (2004), Evidence of the effect of summertime midlatitude convection on the subtropical lower stratosphere from CRYSTAL-FACE tracer measurements, *J. Geophys. Res.*, *109*, D18304, doi:10.1029/2004JD004655.
- Read, W. G., et al. (2007), Aura Microwave Limb Sounder upper tropospheric and lower stratospheric H<sub>2</sub>O and relative humidity with respect to ice validation, *J. Geophys. Res.*, *112*, D24535, doi:10.1029/2007JD008752.
- Rollins, A. W., T. D. Thornberry, R. S. Gao, S. Woods, R. P. Lawson, T. P. Bui, E. J. Jensen, and D. W. Fahey (2016), Observational constraints on the efficiency of dehydration mechanisms in the tropical tropopause layer, *Geophys. Res. Lett.*, *43*, 2912–2918, doi:10.1002/2016GL067972.
- Rothman, L. S., et al. (2009), The HITRAN 2008 molecular spectroscopic database, *J. Quant. Spectrosc. Radiat. Transfer*, *110*, 533.
- Sargent, M. R., D. S. Sayres, J. B. Smith, M. Witinski, N. T. Allen, J. N. Demusz, M. Rivero, C. Tuozzolo, and J. G. Anderson (2013), A new direct absorption tunable diode laser spectrometer for high precision measurement of water vapor in the upper troposphere and lower stratosphere, *Rev. Sci. Instrum.*, *84*(7), 074102.
- Sargent, M. R., J. B. Smith, D. S. Sayres, and J. G. Anderson (2014), The roles of deep convection and extratropical mixing in the tropical tropopause layer: An in situ measurement perspective, *J. Geophys. Res. Atmos.*, *119*, 12,355–12,371, doi:10.1002/2014JD022157.
- Sayres, D. S., L. Pfister, T. F. Hanisco, E. J. Moyer, J. B. Smith, J. M. S. Clair, A. S. O'Brien, M. F. Witinski, M. Legg, and J. G. Anderson (2010), Influence of convection on the water isotopic composition of the tropical tropopause layer and tropical stratosphere, *J. Geophys. Res.*, *115*, D00J20, doi:10.1029/2009JD013100.
- Schmit, T. J., et al. (2013), Geostationary Operational Environmental Satellite (GOES)-14 super rapid scan operations to prepare for GOES-R, *J. Appl. Remote. Sens.*, *7*(1), 073462.
- Schoeberl, M. R., and A. E. Dessler (2011), Dehydration of the stratosphere, *Atmos. Chem. Phys.*, *11*, 8433–8446.
- Schoeberl, M. R., S. D. Doiron, L. R. Lait, P. A. Newman, and A. J. Krueger (1993), A simulation of the Cerro Hudson SO<sub>2</sub> cloud, *J. Geophys. Res.*, *98*, 2949–2955.
- Schoeberl, M. R., A. E. Dessler, T. Wang, M. A. Avery, and E. J. Jensen (2014), Cloud formation, convection, and stratospheric dehydration, *Earth Space Sci.*, *1*, 1–17.
- Schwartz, M. J., W. G. Read, M. L. Santee, N. J. Livesey, L. Froidevaux, A. Lambert, and G. L. Manney (2013), Convectively injected water vapor in the North American summer lowermost stratosphere, *Geophys. Res. Lett.*, *40*, 2316–2321, doi:10.1002/grl.50421.
- Scott, S. G., T. P. Bui, K. R. Chan, and S. W. Bowen (1990), The meteorological measurement system on the NASA Er-2 aircraft, *J. Atmos. Oceanic Technol.*, *7*(4), 525–540.
- Sela, J. (2009), The implementation of the sigma-pressure hybrid coordinate into the GFS, NCEP office note 461, 25.
- Setvák, M., K. Bedka, D. T. Lindsey, A. Sokol, Z. Charvát, J. Štátnka, and P. K. Wang (2013), A-train observations of deep convective storm tops, *Atmos. Res.*, *123*, 229–248.
- Sherwood, S. C., J.-H. Chae, P. Minnis, and M. McGill (2004), Underestimation of deep convective cloud tops by thermal imagery, *Geophys. Res. Lett.*, *31*, L11102, doi:10.1029/2004GL019699.
- Shi, Q., J. T. Jayne, C. E. Kolb, D. R. Worsnop, and P. Davidovits (2001), Kinetic model for reaction of ClONO<sub>2</sub> with H<sub>2</sub>O and HCl and HOCl with HCl in sulfuric acid solutions, *J. Geophys. Res.*, *106*(D20), 24,259–24,274.

- Solomon, D. L., K. P. Bowman, and C. R. Homeyer (2016), Tropopause-penetrating convection from three-dimensional gridded NEXRAD data, *J. Appl. Meteorol. Climatol.*, *55*(2), 465–478.
- Solomon, S., K. H. Rosenlof, R. W. Portmann, J. S. Daniel, S. M. Davis, T. J. Sanford, and G. K. Plattner (2010), Contributions of stratospheric water vapor to decadal changes in the rate of global warming, *Science*, *327*(5970), 1219–1223.
- Smith, J. B. (2012), The sources and significance of stratospheric water vapor: Mechanistic studies from equator to pole, Doctoral dissertation, Earth and Planetary Sciences, Harvard Univ.
- Smith, J. B., E. J. Hints, N. T. Allen, R. M. Stimpfle, and J. G. Anderson (2001), Mechanisms for midlatitude ozone loss: Heterogeneous chemistry in the lowermost stratosphere?, *J. Geophys. Res.*, *106*, 1297–1309.
- Stenchikov, G., R. Dickerson, K. Pickering, W. Ellis Jr., B. Doddridge, S. Kondragunta, O. Poulida, J. Scala, and W.-K. Tao (1996), Stratosphere-troposphere exchange in a midlatitude mesoscale convective complex: 2. Numerical simulations, *J. Geophys. Res.*, *101*(D3), 6837–6851.
- Sun, Y., and Y. Huang (2015), An examination of convective moistening of the lower stratosphere using satellite data, *Earth Space Sci.*, *2*, 320–330.
- Toon, O. B., et al. (2016), Planning, implementation, and scientific goals of the Studies of Emissions and Atmospheric Composition, Clouds and Climate Coupling by Regional Surveys (SEAC4RS) field mission, *J. Geophys. Res. Atmos.*, *121*, 4967–5009, doi:10.1002/2015JD024297.
- Trapp, R. J., N. S. Diffenbaugh, H. E. Brooks, M. E. Baldwin, E. D. Robinson, and J. S. Pal (2007), Changes in severe thunderstorm environment frequency during the 21st century caused by anthropogenically enhanced global radiative forcing, *Proc. Natl. Acad. Sci. U.S.A.*, *104*, 19,719–19,723.
- Trapp, R. J., N. S. Diffenbaugh, and A. Gluhovsky (2009), Transient response of severe thunderstorm forcing to elevated greenhouse gas concentrations, *Geophys. Res. Lett.*, *36*, L01703, doi:10.1029/2008GL036203.
- Van Klooster, S. L., and P. J. Roebber (2009), Surface-based convective potential in the contiguous United States in a business-as-usual future climate, *J. Clim.*, *22*, 3317–3330.
- Wang, P. K. (2003), Moisture plumes above thunderstorm anvils and their contributions to cross-tropopause transport of water vapor in midlatitudes, *J. Geophys. Res.*, *108*, D002581, doi:10.1029/2002JD002581.
- Wang, P. K., S.-H. Su, Z. Carvat, J. Stastka, and H.-M. Lin (2011), Cross tropopause transport of water by mid-latitude deep convective storms: A review, *Terr. Atmos. Ocean. Sci.*, *22*(5), 447–462.
- Weinstock, E. M., E. J. Hints, A. E. Dessler, J. F. Oliver, N. L. Hazen, J. N. Demusz, N. T. Allen, L. B. Lapson, and J. G. Anderson (1994), New fast-response photofragment fluorescence hygrometer for use on the NASA Er-2 and the Perseus Remotely Piloted Aircraft, *Rev. Sci. Instrum.*, *65*(11), 3544–3554.
- Weinstock, E. M., et al. (2006a), Measurements of the total water content of cirrus clouds. Part I: Instrument details and calibration, *J. Atmos. Oceanic Technol.*, *23*(11), 1397–1409.
- Weinstock, E. M., J. B. Smith, D. Sayres, J. V. Pittman, N. Allen, and J. G. Anderson (2006b), Measurements of the total water content of cirrus clouds. Part II: Instrument performance and validation, *J. Atmos. Oceanic Technol.*, *23*, 1410–1421.
- Weinstock, E. M., et al. (2007), Quantifying the impact of the North American monsoon and deep midlatitude convection on the subtropical lowermost stratosphere using in situ measurements, *J. Geophys. Res.*, *112*, D18310, doi:10.1029/2007JD008554.
- Weinstock, E. M., et al. (2009), Validation of the Harvard Lyman-alpha in situ water vapor instrument: Implications for the mechanisms that control stratospheric water vapor, *J. Geophys. Res.*, *114*, D23301, doi:10.1029/2009JD012427.
- World Meteorological Organization (WMO) (1957), Meteorology—A three-dimensional science: Second session of the commission for aerology, *WMO Bull.*, *4*, 134–138.
- Zipser, E. J., D. J. Cecil, C. Liu, S. W. Nesbitt, and D. P. Yorty (2006), Where are the most intense thunderstorms on Earth?, *Bull. Am. Meteorol. Soc.*, *87*(8), 1057.